THE EFFECT OF PORE DENSITY AND DISTRIBUTION ON FATIGUE WEAK LINKS IN AN A713 CAST ALUMINUM ALLOY

Rami A. Almatani
University of Kentucky, ramialmatani@gmail.com
Digital Object Identifier: https://doi.org/10.13023/ETD.2017.148

THE EFFECT OF PORE DENSITY AND DISTRIBUTION ON

FATIGUE WEAK LINKS IN AN A713 CAST ALUMINUM ALLOY

THESIS

A thesis submitted in partial fulfillment of the requirements for the degree of Master of Science in Materials Science and Engineering in the College of Engineering at the University of Kentucky

By
Rami Abdulkarim Almatani

Lexington, Kentucky

Director: Dr. Tongguang Zhai, Professor of Materials Science

and Engineering

Lexington, Kentucky

2017

ABSTRACT OF THESIS

THE EFFECT OF PORE DENSITY AND DISTRIBUTION ON FATIGUE WEAK LINKS IN AN A713 CAST ALUMINUM ALLOY

The effects of pore density and distribution were investigated on the fatigue crack initiation behavior in an A713 sand cast aluminum alloy plate of 12 mm thickness. The applied stress- the number of cycles to failure (S-N) curves of the samples taken from 2 mm and 5 mm from the free surface were obtained using four-point bend fatigue testing at room temperature, frequency of 20 Hz, stress ratio of 0.1, sinusoidal waveform, and in ambient air. The fatigue strengths of both, the 2 mm and 5 mm samples were 60% of the yield strength (σy=171.9 MPa) of the alloy. Optical microscopy, SEM, and EDS mapping were used to characterize pores and particles in 2 mm and 5 mm samples. The average pore sizes of the 2 mm and 5 mm samples were measured to be 10 to 14 μm, and 14 to 32 μm, respectively. The pore number densities in 5 mm and 2 mm samples were comparable, but higher number densities of non-clustered coarse pores (gas pores) were observed in 5 mm samples. The crack population found after fatigue testing showed a Weibull function of stress level. The peaks of strength distributions of fatigue weak link density of 5 mm and 2 mm samples were measured to be 0.017 mm^{-2} at 67.6 % σy, and 0.01027 mm^{-2} at 69.5%

σy. Crack populations, when normalized by number densities of gas pores (non-clustered) and number densities of shrinkage pores (clustered), giving crack nucleation rate (crack/pore, mm^{-2}), showed a good fit with the Weibull function in 2 mm and 5 mm samples. Shrinkage and gas pores could both become the main crack initiation sites (i.e. fatigue weak links) in this alloy. Higher nucleation rates of gas pores and shrinkage pores were observed in 5 mm samples compared to those rates in 2 mm samples. At high applied stresses, the 2 mm samples showed better fatigue lives than those of 5 mm samples. Fractured surfaces were analyzed using SEM and found that the main crack initiation were predominately from pores. The pores on the fractured surfaces were counted and their depth and width were measured. It was found that the cracks may not necessarily initiate from coarse pores, but sometimes from shrinkage pores (i.e. group of pores). The depth from the free surface, the width, the size, and the orientation of pores are key factors in increasing the driving force for crack initiation and subsequently those pores turn into long cracks. Moreover, the aspect ratios of pores on the main cracks were measured and found that in 5 mm samples, some pores have an aspect ratios of less than 0.7, which means that these pores are elongated in depth and have a narrow width which increase the stress concentration on the surface, thus, increasing the driving force for crack nucleation.

KEYWORDS: A713 Cast Al alloy, four-point bend fatigue test, gas pores (non-clustered), shrinkage pores (clustered), fatigue weak links (FWL).

<div align="right">

Rami Almatani
_____

04/28/2017
_____

</div>

THE EFFECT OF PORE DENSITY AND DISTRIBUTION ON FATIGUE

WEAK LINKS IN AN A713 CAST ALUMINUM ALLOY

By

Rami Abdulkarim Almatani

Dr. Tongguang Zhai
Director of Thesis

Dr. Thomas Dziubla
Director of Graduate Studies
Date   04/28/2017

To my parents and my family

ACKNOWLEDGEMENTS

Many people have helped me in my master's degree. I would like to thank them all. Specifically the following:

TABLE OF CONTENTS

LIST OF TABLES

LIST OF FIGURES

Chapter 1 Introduction

Fatigue of materials and fatigue failures are significant issues in engineering applications [1]. The word *fatigue* is used to express human physical status. However, In engineering and in scientific societies, fatigue is a terminology extensively used to describe failures of structures and components that are subjected to cyclic loading [2]. Mechanical fatigue of engineering alloys is a result of externally applied cyclic stresses or strains. Moreover, fatigue failures can lead to a catastrophic tragedy and loss of life [3]. It estimated that the cost correlated directly to fatigue of materials and fracture is significantly high. Several studies in the 1980s indicate that the cost related to fatigue failures and fracture is around $120 billion in the Unites States, which represents approximately 4% of the gross domestic product of the United States [4, 5]. This number may have been increased in the last decade, due to the expansion of production and usage of engineering materials. As a consequence of these numerous effects, attention has been given to fatigue and fracture of materials in the scientific community.

1.1 Historical Overview on Fatigue of Materials Research

The research on fatigue of engineering materials has started in the early 19th century, which emphasises on how and why components fail from fatigue loading [2]. Numerous scientists have studied fatigue failures of engineering alloys. Wöhler, who has conducted analytical and systematic fatigue tests on railroad axles [6]. His tests and studies have characterized fatigue failures in terms of stress-life cycles (S-N) diagrams and introduced the new terminology "endurance limit" or referred as the fatigue limit.

At the time were microscopy was invented, research on fatigue of metals has grown and one of the early studies on fatigue of metals on a microscopic level was done by Ewing *et al.* [7]. The significant findings of Ewing *et al.* were that the cyclic slip bands on a polished sample were visible under optical microscopy. Moreover, these slip bands were continuing to grow upon cyclic loading, leading to nucleation of fatigue cracks. Empirical equations to quantify S-N curves of metals was introduced by Basquin [8]. Basquen showed in his study that the applied stress versus number of cycles to failure has a linear relationship.

The field of fracture mechanics and its theories in fatigue research were extensively studied at the period post World War II era [9, 10]. Pioneering research was conducted by Paris *et al.* [10], who were the first to relate da/dN (fatigue crack growth/stress cycle) to a range of stress intensity factor, ΔK. The effects of microstructural and environmental factors on fatigue behavior including crack initiation and crack growth of engineering materials were given considerable efforts back in the 1950s.

The research on fatigue behavior has progressed significantly because of electron microscopy and its advantages [11]. Among those who have contributed to research on fatigue of materials, were Zappfe *et al.* [12]. They reported the markings on fatigued samples, which are named and known as fatigue striations. Several studies on fatigue striations and the spacing between contingent striations can be found elsewhere [13]. Extrusions and slip roughening are terms observed first by Forsyth [14, 15]. He documented these phenomena in a solution treated Al-Cu alloy and in silver chloride polycrystals.

The presence of microstructural defects in engineering alloys such as inclusions and porosities decrease the fatigue strength and the fatigue life. These defects are considered as preferred crack initiation sites, which depend on several mechanical, environmental and microstructural factors. For example, slip systems of the alloy, the strength of the alloy and the defect, and the interface between the defect and the matrix of the alloy [16]. The microstructural effects on fatigue properties of engineering alloys were documented several decades ago. However, quantitative understanding of microstructural effects on fatigue behavior remains challenging. Thus, further investigations need to be conducted to fully understand fatigue mechanisms.

1.2 Fatigue Behavior of materials

As mentioned in the previous section, studies on fatigue of materials have expanded in the 20th century. These studies reported that the fatigue cracks nucleate at a scale of atomic level and start to grow to the macroscopic level of the material ending in final failure. Figure 1.1, shows two periods exhibited in fatigue life and relevant components that monitor fatigue behavior of materials [1]. It can be seen from Figure 1.1 that fatigue life consists of fatigue crack initiation stage and the fatigue crack growth stage. Fatigue crack initiation period consumes most of the fatigue life of a material. It begins on the free surface of the material along the slip lines leading to fatigue crack nucleation. Typically, crack initiation period is characterized by three main phases, namely, cyclic slip, crack nucleation, and microcrack growth. Long crack growth is mainly under crack growth period.

Fatigue crack initiation usually starts on free surfaces or sub-surfaces of the engineering material. The presence of impurities, inclusions, slags, and precipitates in the material give

rise to fatigue damage. As mentioned earlier, crack initiation period control the fatigue life of a material under high cycle fatigue. Some micro cracks are initiated from the persistence slip bands (PSBs) due to the slip generated from cylic loading, producing extrusions and intrusions which are dipicted in Figure 1.1 [15]. Observations of crack initiation along PSBs have been accredited to Katagiri *et al.* [18]. By using transmission electron microscopy (TEM) to observe dislocations in fatigued polycrystalline Cu, Katagiri *et al.* found that crack initiation and early growth nucleate in the PSBs. These valleys and troughs serve as notches producing stress concentration that can promote more slip and thus, fatigue crack initiation along PSBs. Removing these intrusions and extrusions from the sample surface by means of electropolishing can increase the fatigue life [18].

Two approaches are commonly employed to study the fatigue behavior of engineering materials. The first approach is to characterize fatigue failure by total-life using stress versus cycles to failure curve which is known as S-N curve [6]. Sufficient laboratory samples needed to fully construct the S-N curve. These samples are tested over a range of cyclic stresses under plane bending, rotating bending, tension-tension, or compression-tension. Procedures of these tests can be found in details in ASTM standards [17]. The fatigue limit can be derived from S-N by observing samples that do not fail for an infinite number of cycles under specified stress amplitude. Some engineering alloys such as high strength aluminum alloys and steels, does not show a threshold or a fatigue limit. Thus, the stress amplitude continues to decrease with increasing number of cycles to failure. For this reason, the endurance limit or the fatigue limit is derived from stress amplitude for samples that can withstand for at least 10^7 cycles [2].

The other approach is to characterize fatigue failure based on the resistance to fatigue crack growth which is commonly known as fracture mechanics approach [2]. The primary assumption in this method is that all engineering materials are flawed. Using Paris law, Equation 1.1 [10], one can derive fatigue crack growth rate by plotting da/dN versus ΔK. Both approaches are widely accepted in scientific research.

$$da/dN = f(\Delta K) \tag{1.1}$$

After introducing general overview on fatigue behavior of materials, the primary focus on the following sections will be directed to the fatigue properties of aluminum alloys, and more extensively on fatigue properties of cast aluminum alloys.

1.3 Fatigue Properties of Aluminum Alloys

Due to their strength, corrosion properties, and formability, aluminum alloys primarily have been used in aerospace and automotive applications. Due to the expansion of the applications of aluminum alloys, which operate on services that are under cyclic loading, susceptibility to fatigue failures, are significantly high. Thus, numerous studies were carried out to characterize fatigue strength of wrought and cast aluminum alloys [19-21]. The main focus in the past few decades was to identify and to understand variables that cause fatigue failures in aluminum alloys.

Fatigue failures generally occur under high-cycle fatigue loading at stress levels below the yield strength of an engineering alloy. A number of variables that causes crack initiation and fatigue failure in aluminum alloys are including, but not limited to, microstructural and environmental effect; loading condition; and processing history. Microstructural effects

include grain diameter, porosity, second phase particles, and texture. Environmental effects such as humidity level, temperature, and corrosive environments emerge out as factors that can affect the fatigue properties. Loading condition plays a significant role in affecting fatigue strength e.g. stress ratio, applied stress level, stress range, and the waveform of applied stress. The surface condition, roughness, and manufacturing history in an engineering alloy are examples of processing history that may impair the fatigue properties [22, 23].

Constituent particles are the most detrimental crack initiation sites in wrought aluminum alloys.[24-27]. Simply because these constituent particles are pre-fractured during manufacturing processing (i.e. rolling and extrusion) and the particle-matrix interface is considered weak. Furthermore, particle thickness, aspect ratio, and density were found to be the essential factors affecting fatigue crack initiation and fatigue crack growth [27]. The following sections introduce a literature review on fatigue properties of cast aluminum alloys and the factors that affect the fatigue strength.

1.4 Literature survey on Fatigue Properties of Cast Aluminum Alloys

Cast aluminum alloys have been used in industry for decades, thanks to their superior properties and to their ability to obtain net-shape geometries with dimensional accuracy [28]. The yield strength of cast aluminum alloys ranges from 20 MPa up to 450 MPa [29]. Other properties including weight, elongation percentage, and hardness are reported in the literature. Although cast aluminum alloys are reliable in industrial applications, their fatigue strength and, namely, their fatigue limit, are well below the yield strength. It is believed that the fatigue limit of cast aluminum alloys is one or two order magnitudes lower

6

than the yield strength [30]. This is mainly attributed to casting defects exhibited in cast aluminum alloys and several other factors that may degrade fatigue properties such as dendrite arm spacing (DAS) and eutectic phase. Size, shape, and distribution of intermetallic particles influence the fatigue properties of cast aluminum alloys [31]. One of the major defects in aluminum casting products is the presence of microscale defects called microporosity. The presence of microporosity in the cast play a role in impairing the fatigue lives of cast aluminum alloys [30, 32-34]. The following subsections will introduce the effect of microporosity on fatigue behavior of cast aluminum alloys.

1.4.1 The effect of porosity on fatigue properties of cast Al alloys

One of the major problems in aluminum casting products is the presence of microporosity, which is associated with two primary factors during the casting process. One of them is shrinkage, which is caused by the lack of adequate feeding process during solidification of the molten metal [35]. Commercial cast aluminum alloys exhibit volumetric shrinkage in the range of 5% to 6% during solidification. As the liquid metal casting freezes, the capability to feed the molten metal becomes hard to achieve [34]. Due to the decreasing size of the channels inside the melt, formation of shrinkage porosity (shrinkage pores) becomes easy. Shrinkage pores generally have an irregular, complex morphology, and a crack like features, see Figure 1.3 [36]. The other factor is the presence of gas in the melt, which mainly resulted from the difference in the solubility of hydrogen in the liquid/solid interface, leading to the formation of gas pores [37]. These types of casting defects, affect the mechanical properties and fatigue crack initiation behavior of cast aluminum alloys during service as previously studied in literature [38-40].

Several studies suggest that fatigue cracks are initiated from those pores located at/or near the surfaces of fatigued samples [41, 42]. Lados *et al.,* found in their study that the fatigue life decreases as the fatigue crack initiation pore sizes increases [41]. Factors affecting fatigue properties in sand cast Al-Si-Cu alloy were studied by Kwai *et al.,* [21]. It was deduced from this study that there are three factors controlling fatigue life of B319 Al alloy, namely, crack initiation at shrinkage pore with sharp radii, debonding at the particle-matrix interface, and crack growth along interdendritic grain boundaries. One of the studies concludes that the primary parameter for fatigue crack initiation is due to decohesion of Si particles located at/or near pores that are at/or below the surface of AS7G03 cast aluminum alloy [43]. A finite element model was used by Fan *et al*, to study the effect of particles/pores sizes and morphologies on fatigue crack incubation life using Coffin-Manson criteria [44]. In their study, they concluded that large pores exhibit high plastic strain, which leads to a lower fatigue crack incubation life.

One of the commercial aluminum cast alloys that exhibit casting defects is A713 sand cast aluminum alloy, which is used in engineering applications such as automotive and machinery parts. Previous studies show that the size distribution of pores within the alloy, play a major role in decreasing fatigue lives of cast aluminum alloys. Also, number of crack initiation sites (i.e. fatigue weak links), show a significant degradation in fatigue properties [38]. Zhai [45] has established a method to characterize the strength distribution and population of fatigue weak links, and regarded them as fatigue properties in an AA8090 commercial Al alloy. Yuanbin Zhang *et.al*, [38] have found that the number of fatigue cracks observed on the surface of A713 sand cast aluminum alloy show a Weibull

distribution function with a fatigue limit of 94.5 MPa and the average diameter of pores was 20.13 μm.

Different distributions exhibit in cast aluminum alloys in either random or clustered distribution or combination of random and clustered distribution. Spatial arrangements of microporosity exhibit a significant effect on the mechanical properties of casting alloys as well as pore size and number density that eventually lead to scattering in the S-N curve. It is necessary to quantify the nearest neighbor distances between pores, pore number density, and pore size, to estimate the effect of pores distribution in the alloy. A number of techniques have been developed to measure the average nearest neighbor distances between pores in cast aluminum alloys [36, 46]. The basic techniques used in these studies were to create a montage of large number of contiguous micrographs (field of views of, e.g. 50 micrographs) by using digital image analyzer. It can be recognized that if one can take adjacent micrographs manually, then a problem will arise, namely, edge matching for each next micrograph. Creating a montage gives approximately precise measurements of nearest neighbor distances. To the best of our knowledge, there have been no systematic studies obtained to correlate pores density and distribution of shrinkage and gas pores to crack nucleation rate. Further analysis should be carried out to fully understand the main role of pores in crack initiation and early crack growth.

1.5 Pore Formation Mechanism

The presence of pores in casting alloys has been well studied as a high concentration of microporosity can result in degradation of mechanical properties and specifically, of fatigue properties. Two types of porosity exhibit in cast alloys as mentioned earlier, gas and shrinkage pores. While there are studies explain the formation of microporosity. Still

the physics associated with microporosity formation are complex. It is believed that the main source of microporosity formation (gas pores) in aluminum alloys is the presence of hydrogen in the melt [47]. Moreover, some studies postulate that the principal mechanism of pore formation is due to the reduction in hydrogen solubility during solidification which leads to the formation of gas bubbles, namely, gas pores [36]. On the other hand, as mentioned earlier, shrinkage pores are formed due to lack of interdendritic feeding during the solidification of the mushy zone in an alloy [48].

There are four types of feeding mechanisms as proposed by Campbell which is shown in details in Figure 1.4 [49]. At early stage of solidification, liquid feeding occurs first. The second is mass feeding which may or may not occur, and it is not fully understood. The third is interdendritic feeding, which occurs at the final stages of solidification of the melt and may have central effects that lead to porosity formation. The last feeding is solid feeding, which occurs at the final stage of solidification. Microporosity forms due to the limitation of these feeding mechanisms.

If there is no evidence of gas contamination in the melt and if the feeding is properly carried out, then there will be no porosity found in the cast alloy. However, in engineering practices, castings are complex and those porosities may exhibit in regions that are not well fed. [50-52]. The exact mechanism of pore nucleation during solidification is still not well understood. Nevertheless, some studies explain the formation of pores in aluminum and its alloys based on classical theories of nucleation and growth [35, 53]. The liquid that is flowing towards the root of the dendrites to reduce the volumetric shrinkage exhibits a pressure drop between the mushy zone and the liquid metal [54]. The large difference in

solubility of hydrogen in the interdendritic liquid metal leads to the formation of gas pores. When the molten metal solidifies, hydrogen is rejected from the solid-liquid interface into the liquid phase that becomes enriched in hydrogen concentration. This hydrogen enriched region exhibit a gas pressure that is given by Sievert's law (Equation 1.2) [53]:

$$P_{H_2} = P_{ext} + P_{st} + P_{exp} + \frac{2\gamma}{r} \tag{1.2}$$

Where P_{ext} is the external pressure (i.e. atmospheric pressure), P_{st} is the metallostatic pressure, P_{exp} is the expansion pressure due to the phase transformation exhibited in during solidification, γ is the interfacial energy at liquid/gas interface (i.e. surface tension), and r is the radius of the pore. This approach explains the homogenous nucleation of pore during solidification which is unlikely to occur because the amount of pressure needed for nucleation is high [53].

The other explanation of pore formation is based on the heterogeneous nucleation of gas pores on oxide films, inclusions, and grain boundaries. This is why filtering molten aluminum alloys decreases the amount of porosity in the casting. Anyalebechi [55], carried out experiments on Al-Cu-Mg cast aluminum alloys and found that initial hydrogen melt and the solidification rate play significant roles in pore formation including size, shape, and morphology. As the solidification rate increases, the number density of pores formed during solidification is decreased. This is mainly attributed to: (a) the distance that hydrogen can flow during pore nucleation and growth, (b) time required for pore formation and growth, and (c) hydrogen concentration in the melt for pore growth [56]. It is also concluded from these studies that solidification rate effect on porosity formation is higher at low hydrogen levels. In addition, the size and shape of gas pores depend on the capability

11

of growing pores to resist the pressure exerted by the solid phase. Several studies suggest that adding a grain refiner have a major influence in decreasing pore size and number densities [57, 58]. This is attributed to the increase in the number of nucleated grains in the solid regions during solidification.

1.6 Motivation

There were studies conducted to characterize pore distribution which give a quantitative discrimination between gas and shrinkage pores in AM series of cast magnesium alloys and A356 cast aluminum alloy [36, 46]. Correlation between fatigue behavior and pore density and distribution are rarely seen in literature. Xu et al., [59], have found that the pore position from the free surface of a sample significantly affects the stress concentration which reaches its peak value when the pore intercepts the free surface. Furthermore, their finite element modeling shows that the distance between pores could also increases stress/strain concentration when the spacing decreases. Although the model predicted the stress field around pores, the model only considers two spherical pores within one μm distance apart in a direction perpendicular to the applied stress.

The quantitative effects of pore density and distribution on the fatigue crack initiation behavior in an A713 sand cast aluminum alloy still need to be clarified. In this study, a commercial A713 cast aluminum alloy was taken as an example to study the fatigue properties. Although, it is crucial that the processing parameters that affect pore morphology (i.e. solidification rate and hydrogen content) of the ingot are known to predict pore distribution and size, in this work, the processing parameter are unknown, thus, pore

density and distribution measurements were taken from different location to observe the

differences between these two locations in terms of pore size, density, and distribution.

Figure 1.1 Stages of fatigue failure in engineering materials, after ref. [1].
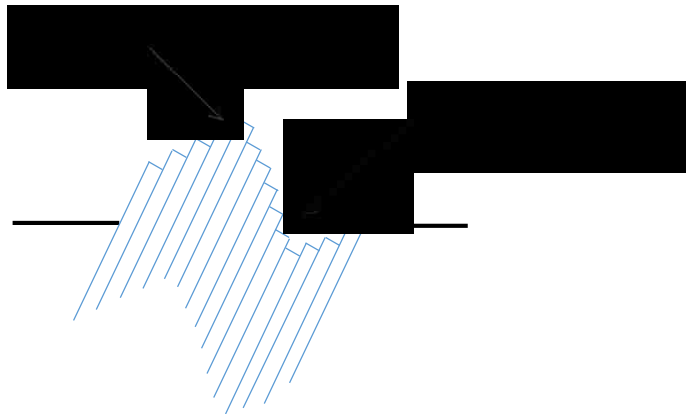
Figure 1.2 The geometry of slip at the material surface; extrusion and intrusion, after ref [15].
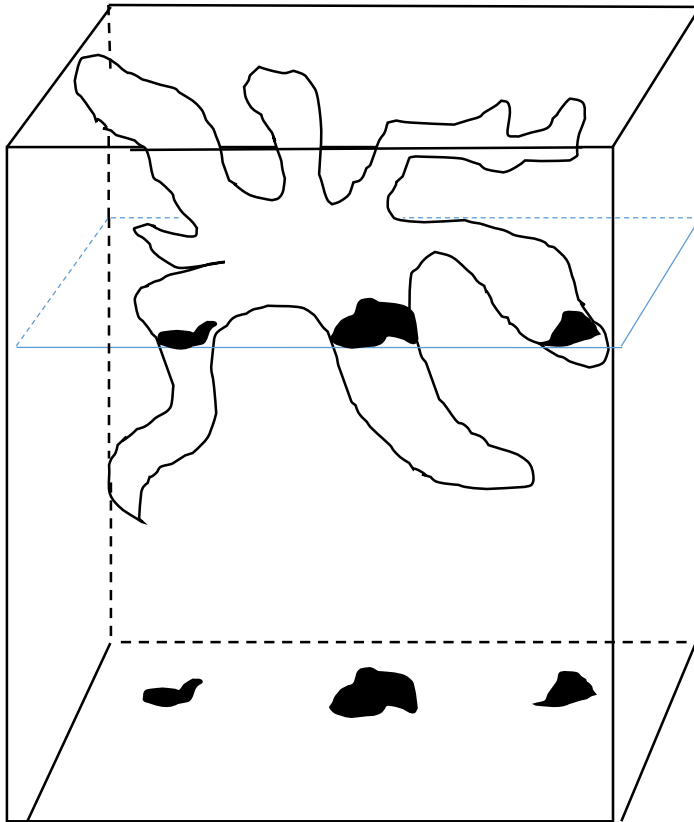
Figure 1.3 Schematic drawing of a shrinkage pore and the resulting two-dimensional image when a sample is sectioned, after ref. [36].
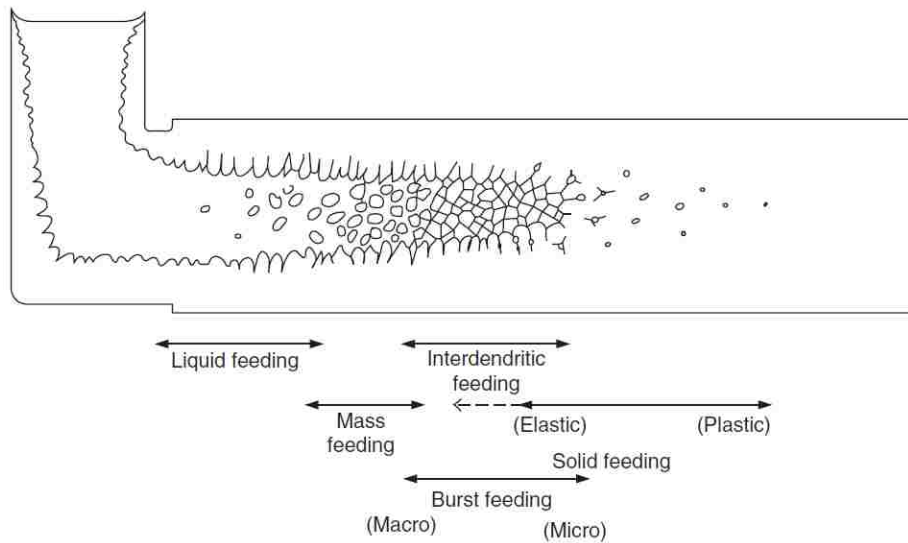
Figure 1.4 Schematic representation of feeding mechanisms in castings, after ref [49].
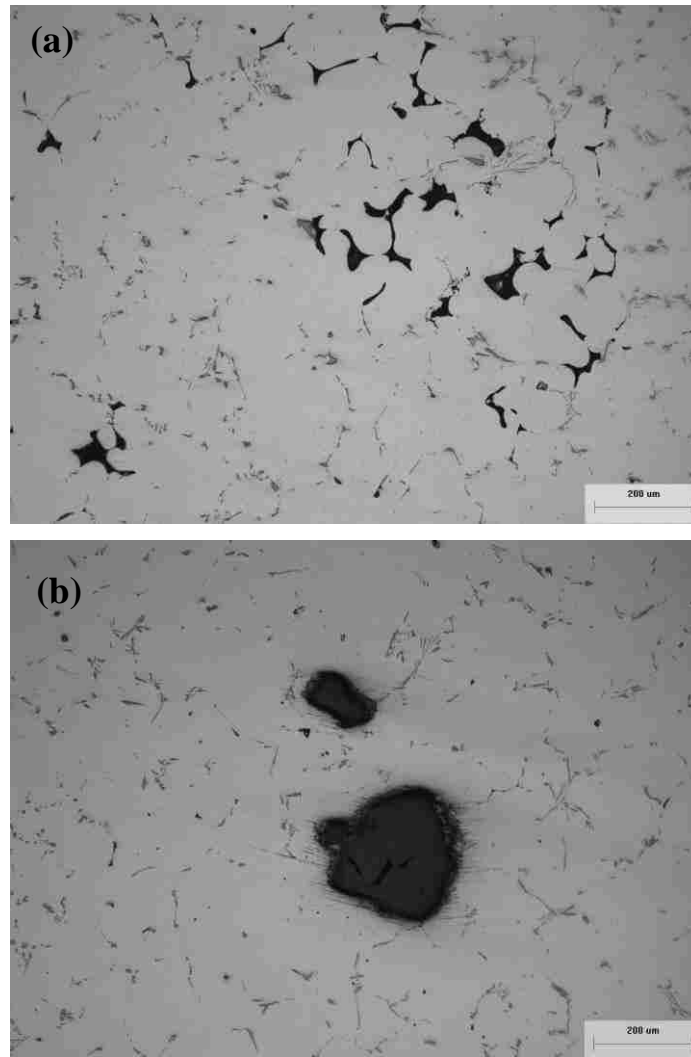
Figure 1.5 Types of pores in an A713 cast aluminum alloy (a) shrinkage pores; (b) gas pores.

Chapter 2 Experimental Material and Methods

2.1 Introduction

In order to quantify the effect of pore density and distribution on fatigue behavior in a cast aluminum alloy, A713 sand cast aluminum alloy was selected in this work.

2.2 Material

The materials were taken from commercial A713 sand cast aluminum alloy that were used to manufacture fan hubs. The nominal chemical composition of the alloy is listed in Table 2.1. The material has yield strength of 171.9 MPa. In this work, samples were cut from the cast blades to the dimensions of 36.5 x 10 x 4.8 mm^3 from two different locations, namely, 2 mm and 5 mm from the surface as schematically shown in Figure 2.1, and Figure 2.2. Samples surfaces were prepared using standard metallographic procedures, in which they were mechanically ground using SiC abrasive papers from grits of 240 to 1200, followed by mechanical polishing using alumina powders (Al_2O_3) as a polishing agent with sizes of 1 μm, 0.3 μm and 0.05 μm and a silica colloidal suspension as the final polishing liquid. Soon after the polishing, the samples were cleaned in alcohol using ultrasonic cleaner to remove any residual contamination from sample preparation. Great care was taken in handling the samples preparation to avoid any damage throughout the work.

2.3 Optical micrographs

Optical microscopy (OM) was employed to study pore sizes and distribution before and after fatigue tests. In each sample, twenty contingent micrographs were taken at 50X magnification before fatigue to in an area of (approximately 60 mm^2) on the surface of the samples to measure nearest neighbor distances and to map all shrinkage and gas pores using digital image analyzer. Micrographs at 50X magnification were taken under optical microscopy to cover the area of 60 mm^2 for simplicity. If the magnification is increased to 100X, 60 micrographs are supposed to be taken from each sample, which is cumbersome work to accomplish. Figure 2.3, shows schematically the location of the micrographs that are located in the area of the sample that is subjected to cyclic stresses.

After that, the twenty micrographs were merged using image software to create a global montage of micrographs for each sample. Particles were removed from the analysis and each pore counted in the segmented global micrograph was numbered for subsequent study after fatigue testing. It is estimated that the error of taking these contingent micrographs in this study is between 2% to 5%. This method assures that edge effect errors of counting pores and measuring nearest distances between pores are minimized. Pore size, number densities, and nearest neighbor distances between pores were counted and measured from each sample and statistically plotted in histograms for comparison. After fatigue tests, fatigued surfaces were examined under optical microscopy at magnifications of 50X, and at 100X and number of cracks (i.e. fatigue-weak links) were counted from each fatigued sample for subsequent analysis.

2.4 Four-point bend fatigue test

Fatigue tests on A713 cast aluminum alloys were conducted in a four-point bend on MTS 810 servohydraulic material testing system, see Figure 2.4. The self-aligning four-point bend fatigue testing geometry and sample dimension are shown previously in Figure 2.2 and in Figure 2.5. [60]. The optimum testing dimensions of the support span/ load span (i.e. L/t), and load span/sample thickness (i.e. t/h) have been reported to be 4 to 5, and 1.2 to 1.5, respectively [60]. This assures a uniform tensile stress on the sample surface for consistent results. The nominal maximum stress on the sample surface is calculated using beam theory:

$$\sigma_{nominal} = \frac{3F(L-t)}{wh^2}$$ (2.1)

Where F is the applied load, t and L are the support span and load span as mentioned earlier, w and h are the width and the thickness respectively. In this study, samples geometry were L×w×h, which equal to 36.5×10×5 mm^3. This advantageous technique is useful in studying fatigue damage (i.e. fatigue weak-links) by means of optical microscopy and scanning electron microscopy. The fatigue tests were carried out on the studied samples at a stress ratio of (R = $\sigma_{min}/\sigma_{max}$=0.1), a frequency of 20 HZ, at room temperature in ambient air, and in a sinusoidal waveform. The fatigue tests were set to run out at 5,500,000 cycles in the stress-cycles measurements. 11 Samples from each batch were tested at different maximum cyclic stresses ranging from 60% to 110% of the yield strength of A713 cast Al alloy (σ_y =171.9 MPa). To study the fatigue crack initiation for these samples, the fatigue tests were terminated when the sample deflection exceeded 10% of the maximum cyclic stress. This

method ensures and minimizes long crack growth in the samples as much as possible. After the fatigue test, the sample surface remains relatively flat in order to examine the fatigue crack initiation sites under optical microscopy.

2.5 Scanning Electron Microscopy (SEM)

Scanning electron microscopy is one of the microscopic techniques that generates high-resolution images and identify the chemical composition of a sample using energy-dispersive spectroscopy (EDS) with high energy electron beam ranging from 0.5 to 30 keV.[61]. The electron source leveraged in the SEM can be a tungsten filament, LaB6, or Schottky emitter [62]. Furthermore, SEM can provide several information about a sample when bombarded by electrons, which generate signals such as secondary electrons (SE), backscattered electrons (BSE), x-rays, and Auger electrons. Figure 2.6 shows the generated signals when an incident beam bombards a sample.

The most frequently used signal is the secondary electrons, which are defined as energies less than 50 eV. These electrons are sensitive to sample surface topography, i.e., observation of texture and surface roughness within a nanometer scale and they are detected by scintillator-photomultiplier and the produced signals are transformed into an intensity distribution which can generate digital images [62].

On the other hand, backscattered electrons are defined as those electrons that undergone several scattering events with an energy higher than 50 eV [63]. Atoms with higher atomic numbers (Z number) have more positive charges on their nucleus, and consequently, more electrons produce elastic collisions, which generate backscattered signals. Characteristic

x-ray signals are also emitted from sample surface when bombarded by an incident electron beam that can provide valuable qualitative and quantitative information such as chemical composition and elemental mapping.

In this study, secondary electron (SE), energy dispersive spectroscopy (EDS), and elemental mapping were used for pore and particles imaging, chemical composition analysis, and fracture surfaces on FEI Quanta 250 SEM, and Zeiss EVO MA 10.

Table 2.1 Chemical composition of A713 sand cast aluminum alloy (in wt. pct.).

Material	Fe	Cu	Mg	Zn	Aluminum
A713 cast Al alloy	1.1	0.1-1.0	0.2-0.5	7.0-8.0	Balance
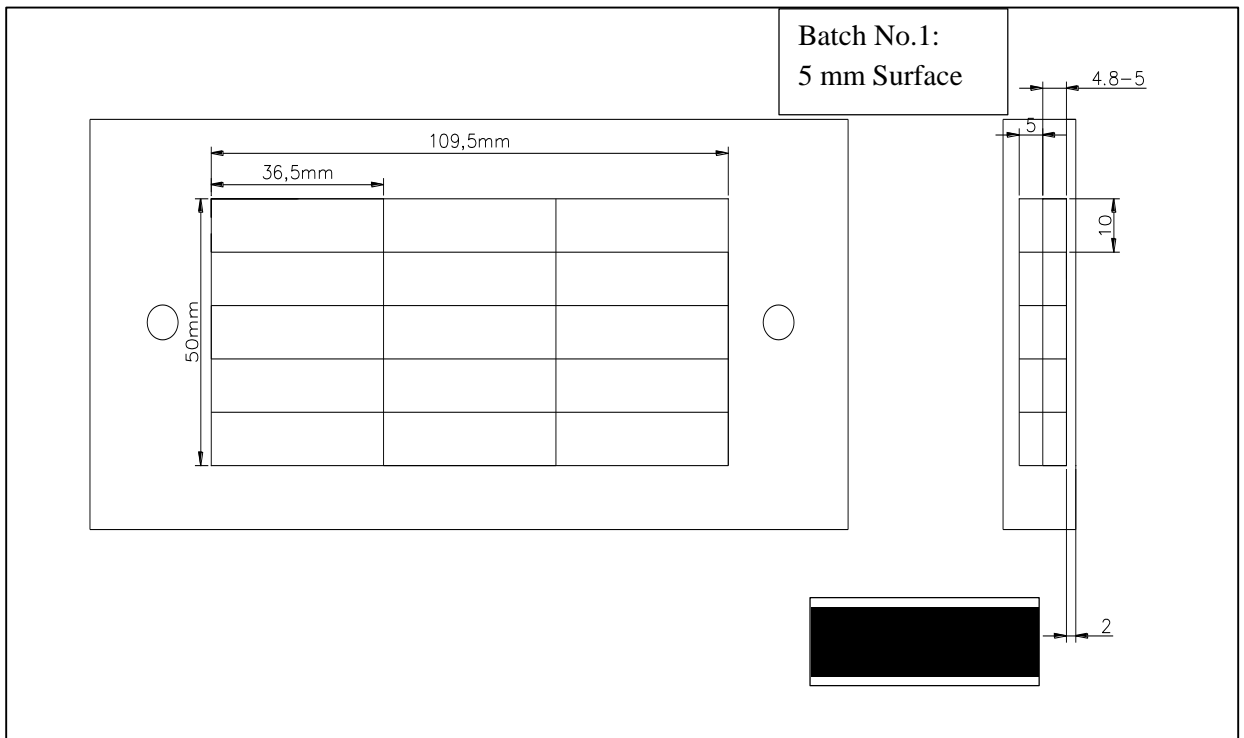
Figure 2.1 Schematic drawing for samples location.
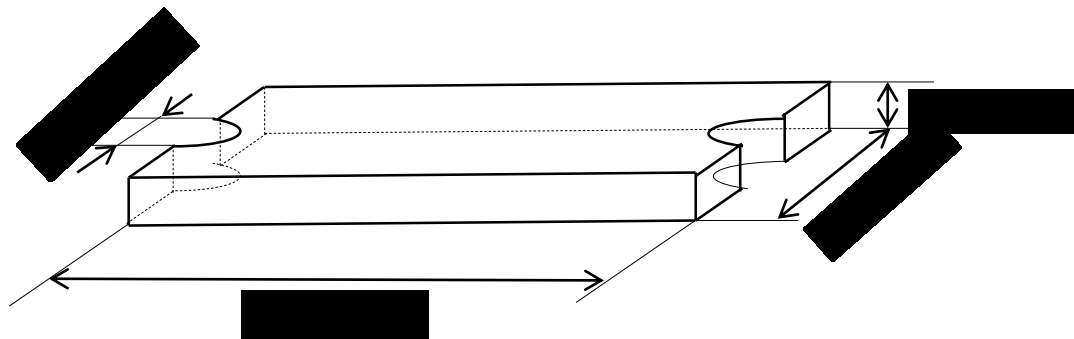
Figure 2.2 Geometry and dimensions of a four-point bend fatigue sample.
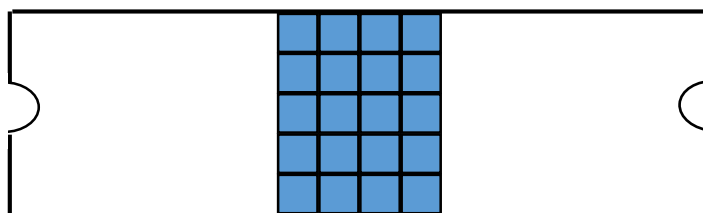
Figure 2.3 Schematic representation showing optical micrographs locations; the surface of the sample that is subjected to fatigue loading.

Figure 2.4 MTS 810 servohydraulic material testing system, the square shows the four-point bend fatigue testing rig.
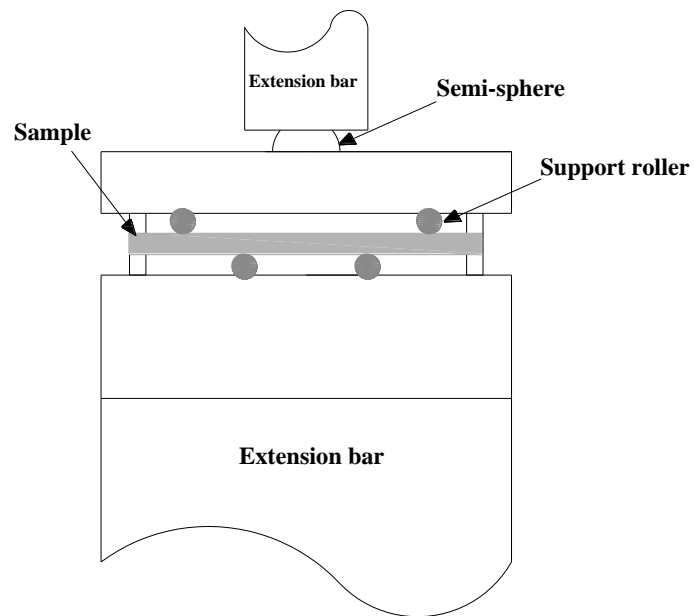
Figure 2.5 Testing geometry of the four-point bend rig test.
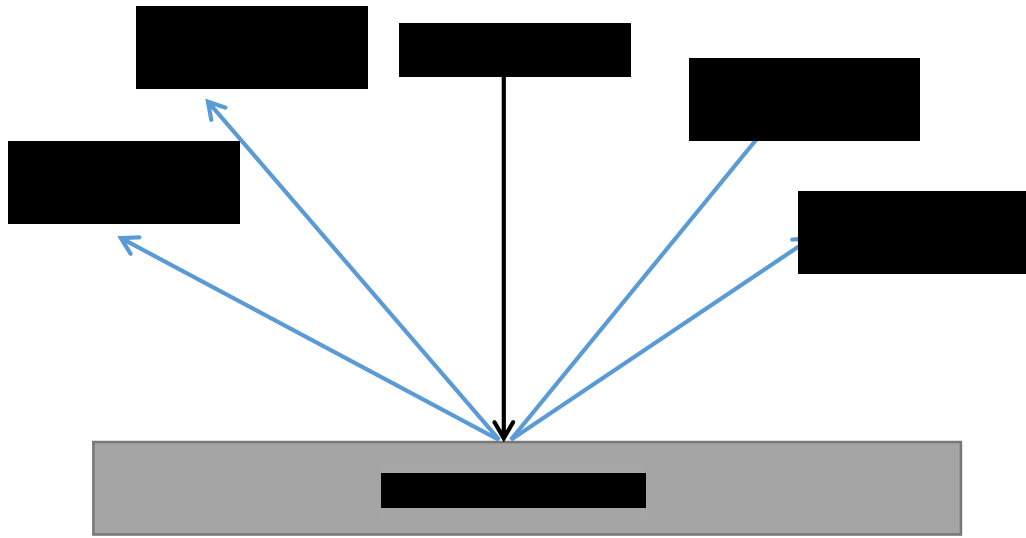
Figure 2.6 Generated signals produced when incident beam bombards a sample.

Chapter 3 Results and Discussions

This chapter represents the primary results and discussions of the effect of shrinkage and gas pores on fatigue behavior in A713 cast aluminum alloy. The previous study was conducted on the same alloy, but still, the effects were not fully understood. Detailed optical micrographs, S-N curve, pore size distribution, pore number density, average nearest neighbor distances between pores, SEM images, and fractography, all included in this chapter.

3.1 Optical micrographs

From the two surfaces; 2 mm and 5 mm samples, optical micrographs reveal and show that pores have different sizes, distribution, and morphology. Figure 3.1 shows two different types of pores in terms of sizes and location. It can be seen that shrinkage pores (i.e. pore clusters) were observed on both surfaces with different sizes and densities. The grain structure of this alloy has been reported in the previous study, which indicates that this alloy has coarse grain structure [38]. Small dispersed rounded gas pores were observed on some of the 5 mm samples.

In this study, as mentioned earlier, twenty micrographs from each sample were taken at 50X magnification to create a montage of global images for each sample. From these global images, pore sizes, pore number density, and nearest neighbor distances between pores were counted. Magnifications of 100X, 200X, and 500X were taken for subsequent analysis. The following sections present the global micrographs including the statistical results for each sample in 2 mm and 5 mm surfaces.

3.1.1 Pore size, density, and distribution

Figure 3.2 and Figure 3.3; show examples of global micrographs of 2 mm samples. Clearly, it can be seen from these figures that the majority of pores are shrinkage pores and tend to have random and clustered distribution. On the other hand, some of the 5 mm samples exhibit some coarse gas pores as shown in Figure 3.4 and Figure 3.5. From these figures, coarser pores are predominately observed in 5 mm samples. The cast blade has a significant segregation in terms of pore size and distribution. Figure 3.6 shows the cross sectional view of the cast blade; it is clear that the pores are segregated in depth and in the longitudinal direction. Different types of pores observed; coarse and fine pores; clustered and non-clustered pores, within the alloy.

Figure 3.7 shows the statistical analysis for pore mean diameter and number densities in 2 mm samples. 11 samples were tested at different stress levels as mentioned earlier. Sample No. 2 mm-12 shows the highest pore number density and average pore diameter of 25.7 per mm^2 and 14 μm, respectively. The average pore size of the 2 mm samples was between 10 to 14 μm; this is true for at least the areas that are under cyclic loading. Pore number densities were different from sample to sample, ranging from as high as 25 per mm^2 to as low as 8 per mm^2. Figure 3.8 represents the statistical results for pore mean diameter and pore number densities in 5 mm samples. It is clearly shown that pores in 5 mm samples are coarser compared to those in 2 mm samples. Average mean pore diameter in 5 mm ranges from 14 μm to 32 μm. Some pores exhibit pore sizes as high as approximately 400 μm in diameter. Pore number density in 5 mm samples differs from sample to sample, similar to those observed in 2 mm samples, ranging from 7 per mm^2 to 24 per mm^2. The pore number density that is larger than 100 μm in size on 5 mm samples were around 4 to 5 per mm^2

which were higher than those observed in 2 mm samples by a factor of 2. These coarser pores found in the 5 mm samples were nucleated in the middle of the blade and it can be attributed to the solidification time and initial hydrogen content in the melt. These gas pores might be trapped during solidification and, thus, there was no sufficient time for these pores to escape to the surface of the blade. Tables 3.1 and table 3.2 summarize the statistical results for 2 mm and 5 mm, which include the area fraction of pores, and nearest neighbor distances between pores; nearest neighbor distances will be discussed in the following subsection.

3.1.2 Nearest neighbor distance of pores

From the global micrographs shown earlier, first nearest neighbor distances between pores were counted using image software. Figure 3.9 represents the histograms of nearest neighbor distances between pores in 2 mm samples that were tested at high stress levels. Sample 2 mm-12 shows an average nearest neighbor distance of 65 μm, while sample 2 mm-6 has an average nearest neighbor distance of 106 μm. For 5 mm samples, shown in Figure 3.10, the nearest neighbor distances for the largest and smallest measured to be 127 μm and 62 μm, respectively. The higher the number density, the smallest the average nearest neighbor distances, which are indeed clustered but in relatively random distribution.

This method does not reflect the whole image of gas pores and shrinkage pores. Since shrinkage pores observed as a group of pores within one entity, one should count those pores and regard them as one shrinkage pore (cluster). The crack nucleation rate, which will be discussed later, were normalized based on number of gas pores and number of

shrinkage pores. Shrinkage pores were counted based on the distance between pores that are between 10 to 50 µm, thus, a group of pores were counted as a one shrinkage pore.

3.1.3 Eutectic Particles

Eutectic phase in A713 aluminum alloy, depicted in Figure 3.11, were analyzed using EDS mapping. The optical micrograph in Figure 3.11(a) clearly reveals the eutectic particle, and they are indicated by arrows. Figure 3.11(b) shows the SEM image of the particle and the subsequent EDS mapping are shown below as well. From Figure 3.11 (e), it is evident that this phase contains traces of Fe and it can be regarded as Fe-containing particle. The morphology of the Fe particle is scripted-like structure, and also there were elongated Fe particles exhibited in this alloy. The size and morphology of these particles were not analyzed in this study, as it focuses only on pores and their effects on fatigue properties.

3.2 S-N curves

As shown in Figure 3.12 the S-N curves of the 2 mm and 5 mm samples were measured by four-point bend fatigue testing, and their fatigue limits were determined to be σ_0=102 MPa. The fatigue limits for both samples were the same, and that pore number density and pore size may not affect the fatigue life at very low stresses when the values of pore density and pore size are low. Also, this is may not be true if other microstructural factors are taken into account such grain sizes and particle structures that could change the fatigue limit of the alloy. These factors mentioned, also could affect fatigue crack initiation and fatigue crack growth.

At higher stress levels, the 2 mm samples show better fatigue lives compared to those in 5 mm samples, except the 5 mm sample that was tested at 121% σ_y. This is largely attributed to the fact that pore number densities and pore size are finer in that sample compared to other samples in 5 mm. One can see in Figure 3.12, approximately a linear relationship between the maximum applied stress and logarithmic number of cycles to failure.

3.3 Crack population vs. stress level

The crack populations formed on the surfaces of 2 mm and 5 mm samples were counted. The crack density is increased with increasing the applied stress until it reaches saturation at or close to the ultimate tensile strength, in other word, the higher the applied stress, the higher the crack densities. Cracks were predominately nucleated at pores, as shown in Figure 3.15 and Figure 3.16.

 Figure 3.15(a) shows multiple fatigue crack nucleation sites (i.e. fatigue weak links) on 5 mm sample surface initiated from pores at a high stress level (maximum cyclic stress= 110% σ_y). On the other hand, lower fatigue crack nucleation sites were observed, shown in Figure 3.15(b); at a lower stress level (maximum cyclic stress= 65% σ_y). This is also true for the 2 mm samples, which can be seen in Figure 3.16.

 Figure 3.16(b) shows clustered pore that contains a crack, and this is crack nucleated along the pore network of these clusters. Gas and clustered pores were predominately the main crack initiator in this alloy.

The fatigue weak links can be measured and plotted against applied stress levels using Weibull distribution. A similar method was used in AA8090 Al–Li, 7075 Al, and A713 [27, 38, 45]. The Weibull function was used to fit crack density vs. stress level:

$$N = N_0 \left(1 - \exp\left[-k \left(\frac{\sigma - \sigma_0}{\sigma_0} \right)^m \right] \right) \qquad (3.1)$$

Where N_0 is the maximum number of cracks that can be observed on the sample surface per mm^2 at a stress level close to the ultimate tensile strength σ_{uts}; k is a constant; and m is the Weibull modulus.

Constant k and Weibull modulus m can be determined by fitting the curve of crack population vs stress level using Weibull function. In this work, N_0 for the 2 mm and 5 mm samples were measured to be 31 and 42, respectively. Figure 3.13 represents the crack populations against the applied stress levels for the 2 mm, and 5 mm samples and plots were fitted using the 3-parameter Weibull function (Eq.3.1). It is evident that the crack densities on the 5 mm samples were higher than those counted on the 2 mm samples by 35% at a stress close to the ultimate tensile strength. From this observation, one can deduce that gas pores with coarse sizes and cluster pores play a major role in crack initiation in the 5 mm samples. Although, fatigue cracks population at an intermediate stress level were relatively similar on 2 mm and 5 mm samples, the main difference was the presence of coarse gas pores on those samples tested at high stress level in the 5 mm samples. It is believed that the A713 sand cast aluminum alloy shows scattering in data in crack population vs. stress level curve. This scattering is due to the size, density and distribution of pores exhibited in the A713 alloy, specifically gas and clustered pores and other

constituents such as eutectic particles. Other factors may contribute to the scattering in data such as microstructure heterogeneity and average grain diameter [38].

If the crack densities are normalized by pore density of gas pores and shrinkage pores, which gives crack nucleation rate (crack/pore, mm^{-2}), the curves fit with Weibull function for both 5 mm samples and 2 mm samples. The crack nucleation rates in 5 mm samples could be fitted using Weibull function as shown in figure 3.17(a). The main crack nucleation sites in these samples are gas pores and shrinkage pores (clustered). Figure 3.17(b) shows the crack nucleation rates in 2 mm for gas and shrinkage pores. The non-clustered pores in figure 3.17 (b) shows a lower nucleation rate compared to those exhibited in 5 mm samples. This may be attributed to the fact that gas pores in 5 mm samples are coarser than those in 2 mm samples. Moreover, the crack nucleation rates of clustered pores in 5 mm and 2 mm samples have higher rates compared to the crack nucleation rates of gas pores in 5 mm and 2 mm samples

3.3.1 Strength distribution of fatigue weak links

Figure 3.14 shows the corresponding fatigue weak links density and the strength distribution of fatigue weak links in 5 mm and 2 mm samples. The strength distribution of fatigue weak links can be measured and quantified from crack population vs. stress level curve. By taking the derivative of Weibull function, the strength distribution of fatigue weak links can be estimated by the following equation [45]:

$$n = CN_0 \left(\frac{km}{\sigma_0}\right)\left(\frac{\sigma - \sigma_0}{\sigma_0}\right)^{m-1} \exp\left[-k\left(\frac{\sigma - \sigma_0}{\sigma_0}\right)^m\right] \qquad (3.2)$$

Where n is the population of fatigue weak link at a specific stress level σ, and C is a scaling constant. N_0, can be quantified by the following:

$$N_0 = \int_0^{+\infty} n d\sigma \qquad (3.3)$$

The characteristic strength distribution of fatigue weak links (n), and fatigue weak link density (N_0), can be regarded as a fatigue properties of a material and the same method was used to characterize the strength distribution in AA8090 Al–Li, 7075 Al, and A713 [27, 38, 45]. As shown in Figure 3.14, the peak of fatigue weak link density and the strength distribution of fatigue weak links in 5 mm and 2 mm samples were measured to be ≈ 0.017 mm^{-2} and 0.0127 mm^{-2}; 67.6% and 69.5%, respectively. This is may be attributed that the 5 mm samples have different types of pores and sizes. Pore number density, pore size, and depth in surface, together are main factors in fatigue crack initiation process. To get better fatigue behavior, the peak of fatigue weak link density should be narrow and low, the fatigue weak link density should be small, and the strength of the fatigue weak link density should be high [45].

3.4 Pores after fatigue tests

From the results presented earlier, the fatigue cracks nucleated from pores with different types; shrinkage pores (clustered) and gas pores (non-clustered). As shown in Figure 3.18, the optical micrographs were merged to observe the main crack path and crack initiation before and after fatigue test. Figure 3.18(a) is the optical micrographs for one of the 2 mm samples that was tested at 110% σ_y (sample No. 2 mm-10), which exhibits clustered pores.

The main crack path and crack nucleation were from those pores, which can be seen in Figure 3.18(b). Figure 3.19 shows optical micrographs for 5 mm sample that were tested at 100% σ_y (sample No. 5 mm-6), which contains pores that are coarse or in other word non-clustered as mentioned previously. The crack initiated from these coarse pores as well as clustered pores. In Figure 3.19(b), one of the cracks is visible, and it was initiated from a gas pore. From Figure 3.19(b), tortured surface is observed due to high stress level applied to the sample and a combination of the presence of clustered and non-clustered pores.

3.5 Fractography

As discussed above, the observed crack initiations were predominately from pores. Figure 3.18(c), shows the typical fracture surface for the 2 mm sample that was mentioned in the previous section. The SEM micrograph reveals one of the pores that nucleated a crack and the fracture steps. Generally, cracks were initiated from pores that are located on surface or subsurface of the fatigued sample. The crack initiation site are marked by red dashed line. Figure 3.19(c) shows the fracture surface of fatigued 5 mm sample. The coarse pore was one of the crack initiators in this sample, which has a depth more than 1000 micron. These elongated coarse pores act as stress concentrators, which increase the driving force for crack initiation. The higher the stress level, the higher the crack initiation. This is evident as multiple pores turn into cracks that are shown in Figure 3.20. This figure shows the SEM micrographs of sample 2 mm-10 at a stress level 110% σ_y. From this figure, one can see the fatigue crack initiation sites are from those pores that turned into long cracks. Multiple pores turned into cracks and those pores depth sizes were measured, which are shown in table 3.3. From table 3.3, is it clear that the depth of these pores are large ranging

34

from 500 to 1000 microns for this sample. Figure 3.21 shows the SEM micrographs for sample 2 mm-12, which was tested at 100% σ_y, multiple pores turned into cracks and this sample exhibits the highest number of pores observed on SEM micrographs. This is can be obvious since its pore number density is 25 per mm^2. The depth of these crack initiators were from 130 to 700 microns.

Figure 3.22 and Figure 3.23shows the SEM micrographs for samples 5 mm-13 and 5 mm-6, which were tested at 110% and 100%, respectively. Those samples have a relatively large pore depth sizes compared to those in 2 mm samples. Several pores have depth size larger than 1000 microns, which increase the crack initiation driving force and these pores are shown in Figure 3.22(d) and (e) for sample 5 mm-13 (110% σ_y), and Figure 3.23(b) and (c) for sample 5 mm-6 (100% σ_y).

3.6 Summary of results and discussion

The results presented above illustrate the critical role of pores as a crack initiation sites. Pore number density, pore sizes and, distribution in depth or on the surface, are contributing factors, which reflect the driving forces for crack initiation and early crack growth. With the presence of clustered and non-clustered pores, coarser non-clustered pores might turn into cracks and those pores could affect the crack nucleation rate. The results show that pores are segregated in depth, and coarser pores might be found inside the alloy, suggesting that those pores were trapped during solidification of the melt. The higher the stress level, the higher the crack initiation tendency.

Crack population vs stress level showed a Weibull type function. Although, the crack population curve in some degree fitted with Weibull function, the normalized curve which gives the crack nucleation rate, shows a good fit in 5 mm samples and in 2 mm samples. Higher crack nucleation rates exhibited in 5 mm samples for gas and shrinkage pores compared to those in 2 mm samples. This observation might suggest the main difference between clustered and non-clustered pores in term of crack nucleation rates and those clustered pores were predominately the main crack initiators in 2 mm samples as well as 5 mm samples. In addition, non-clustered pores in 5 mm samples were coarser than those in 2 mm samples. The 3-dimentional effects of pores play major roles in fatigue crack initiation. Aspect ratios of pores with value less than 1 means that these pores are elongated in depth and have narrow width. This increases the driving force for crack nucleation
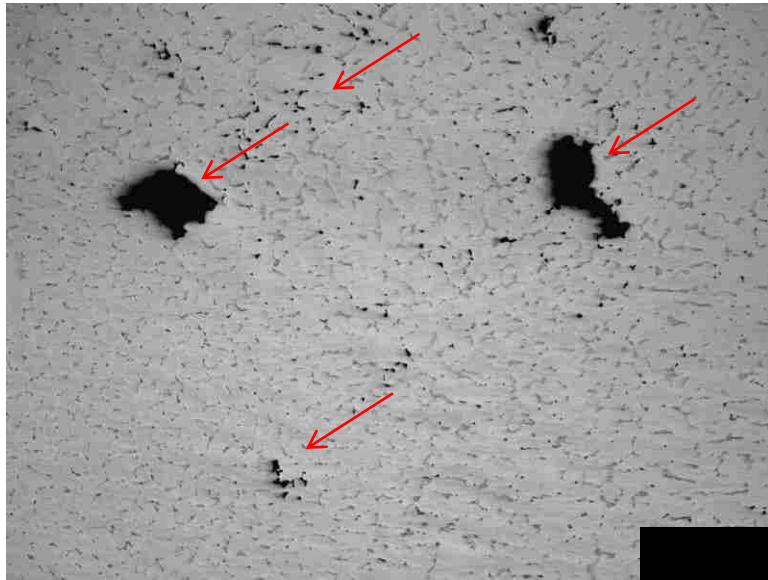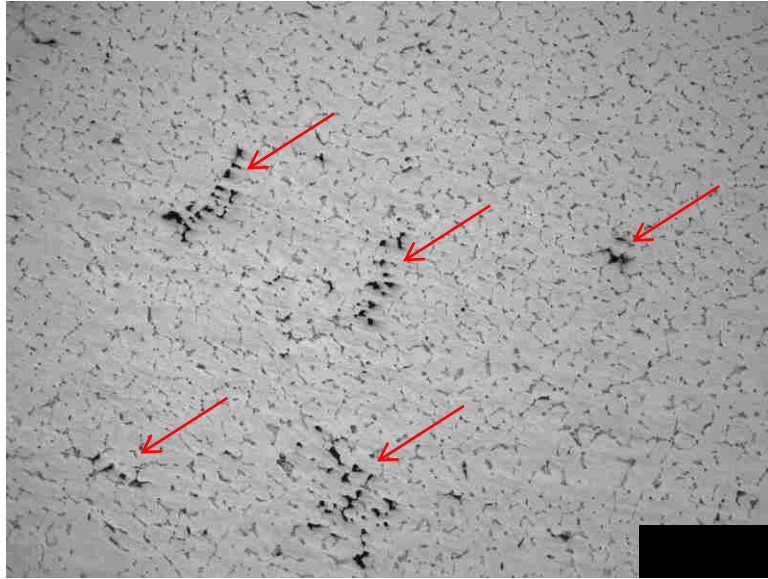
Figure 3.1 Optical micrographs showing pores in: (a) 2 mm surface and; (b) 5 mm surface, arrows indicate pores which have black contrast. Coarse pores in 5 mm surface are considered as non-clustered pores or regarded as gas pores.
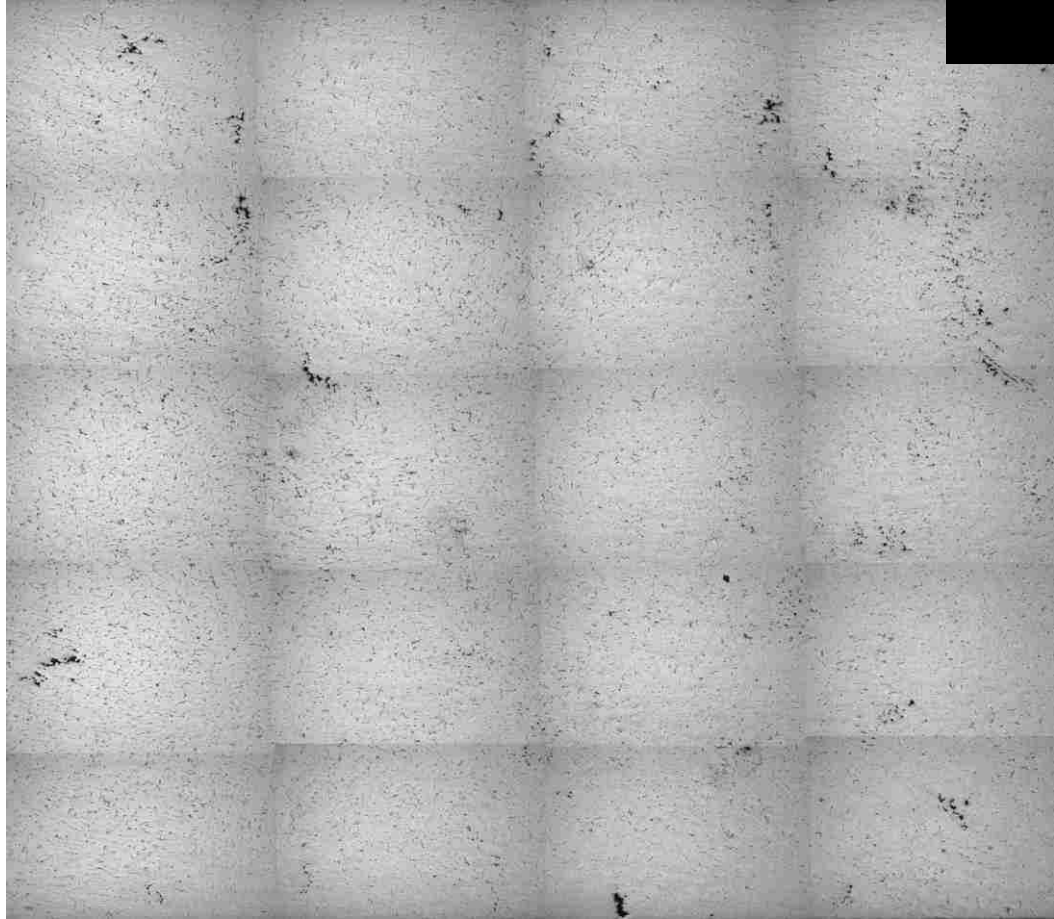
Figure 3.2 Global micrograph showing the pore distribution in one of the 2 mm samples, this global micrograph represents the area under the cyclic stress.
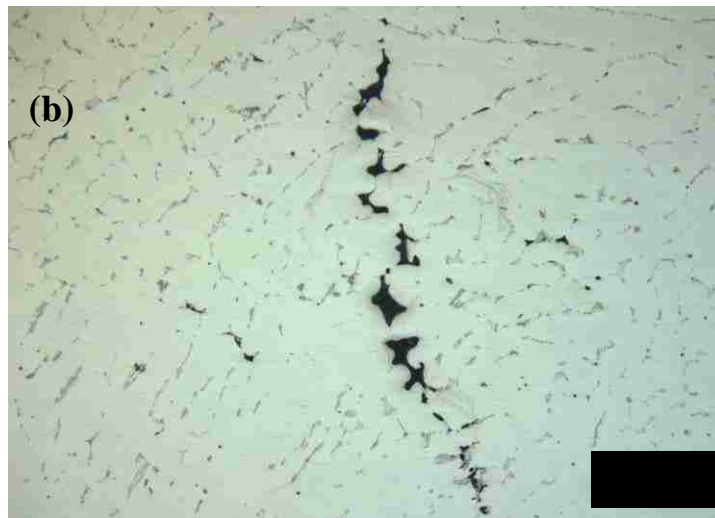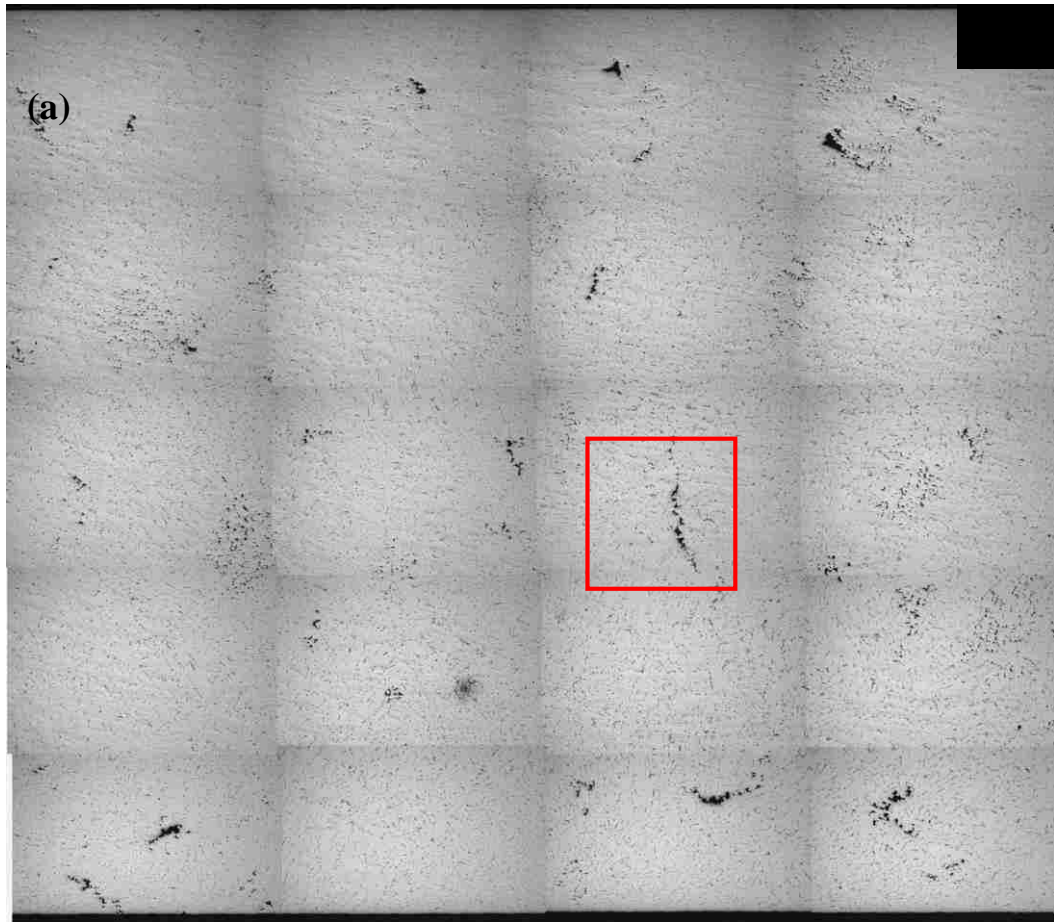
Figure 3.3 Global micrograph showing pore distribution, (a) global micrograph of a 2mm sample; (b) pore structure at 200X magnification, eutectic phase is visible.
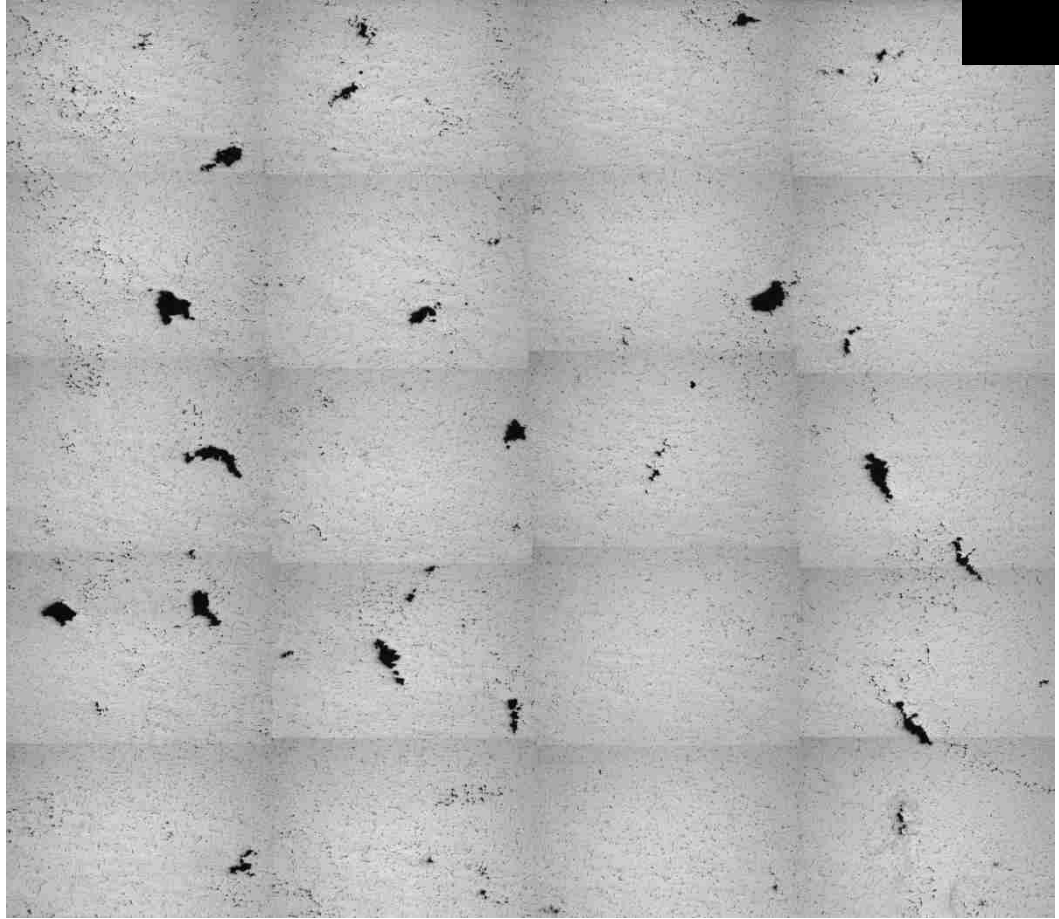
Figure 3.4 Global optical micrograph showing pore distribution in one of the 5 mm samples; sample No. 5 mm-6.
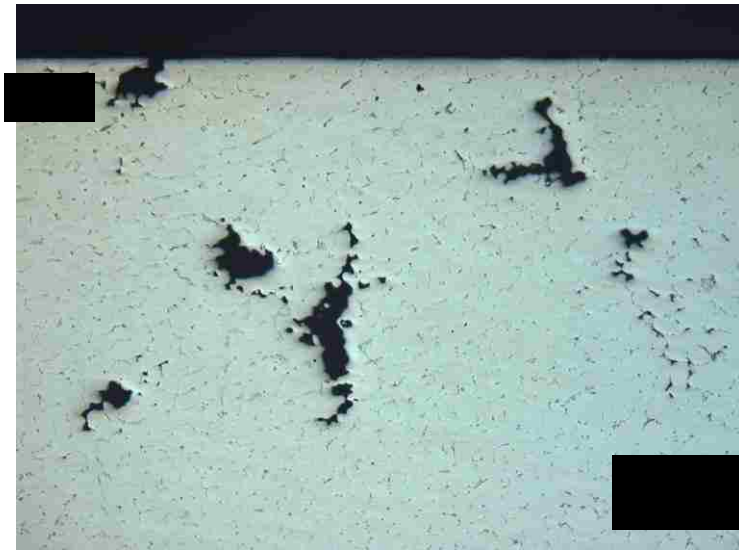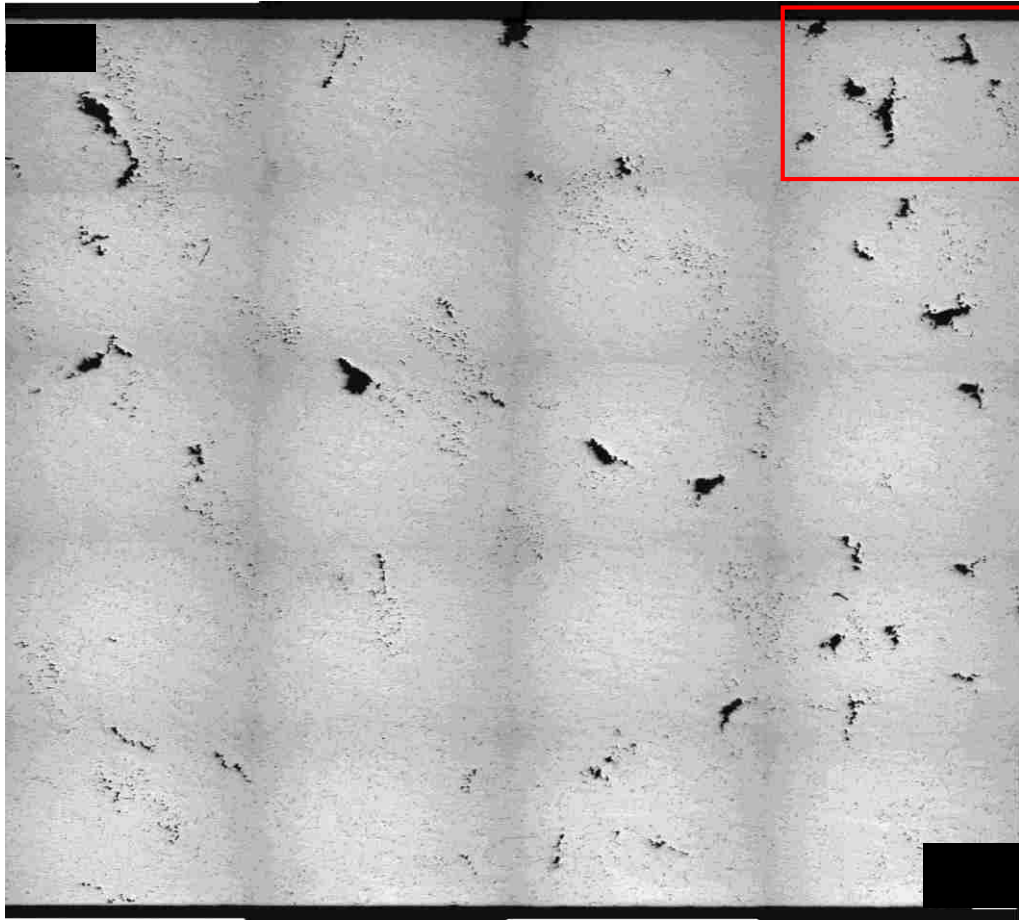
Figure 3.5 Pore distribution on one of 5 mm samples; (a) global
micrograph of sample No. 5 mm-10; (b) micrograph of the upper
right region of the global micrograph.
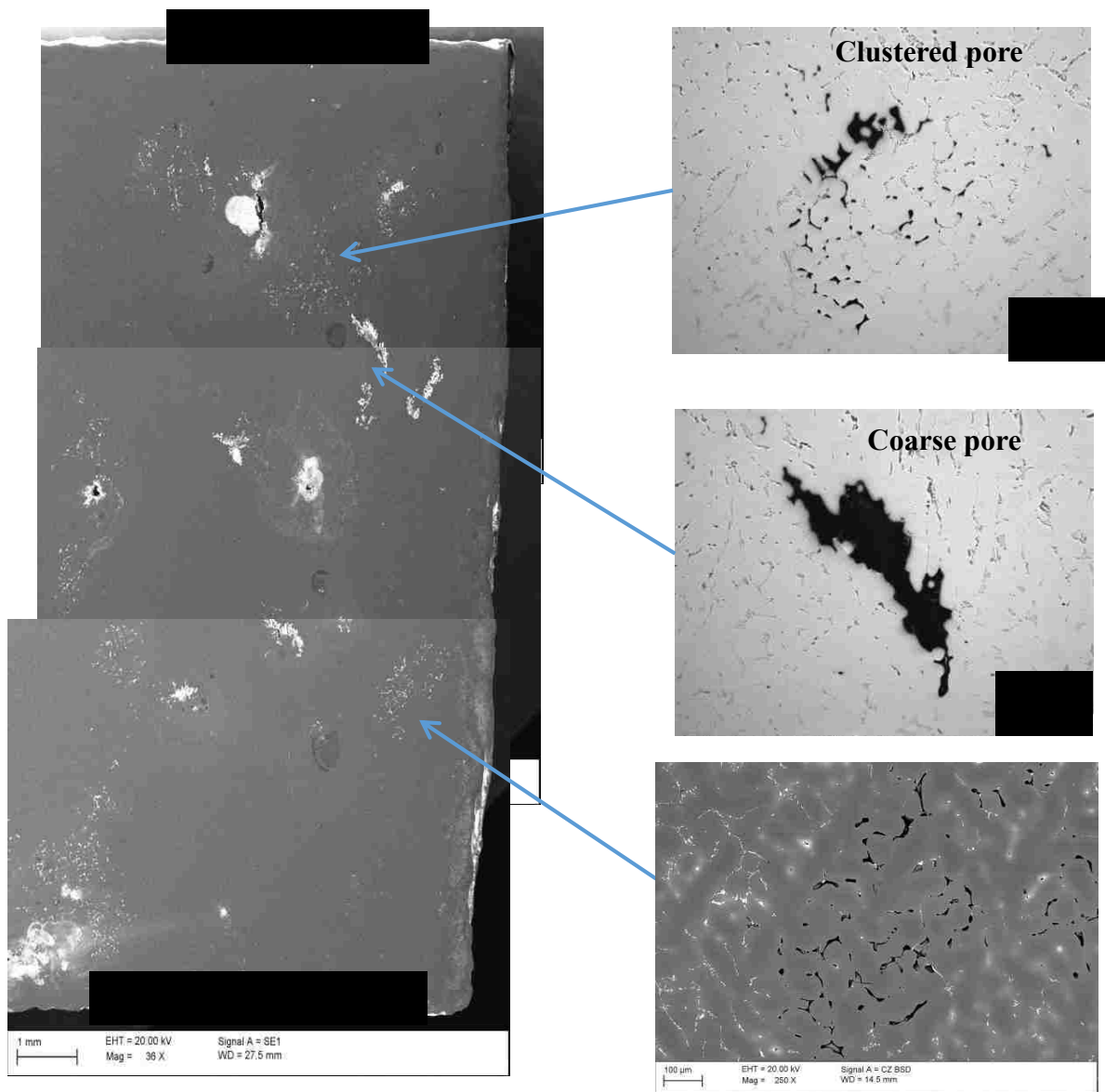
Figure 3.6 SEM and optical micrographs of the cross-sectional view of the blade, clustered and coarse pores are visible.
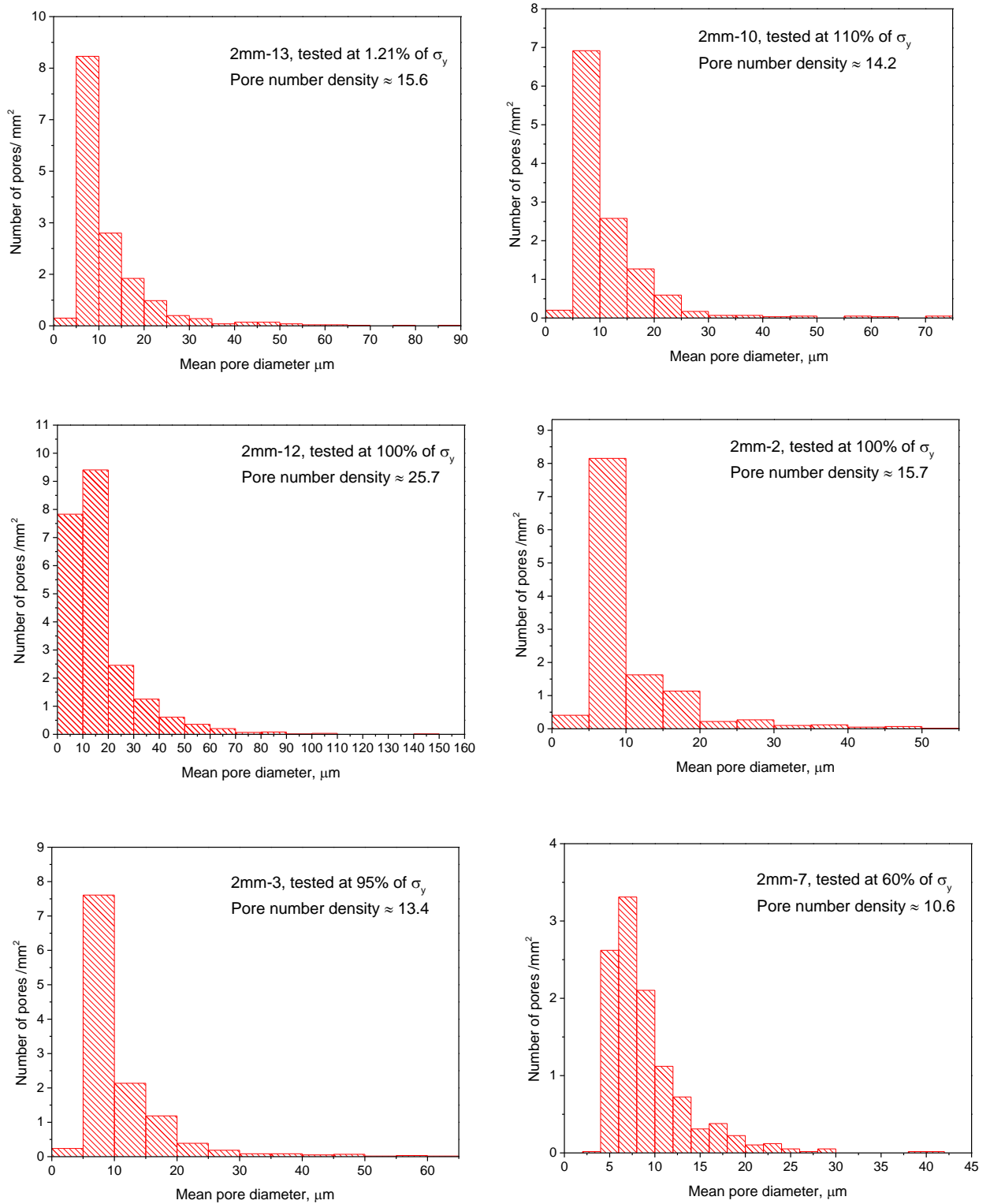
Figure 3.7 Mean pore diameter and number densities of 2 mm samples that were tested at high stress level, sample No.7 tested at 60% of yield stress, which is the fatigue limit.
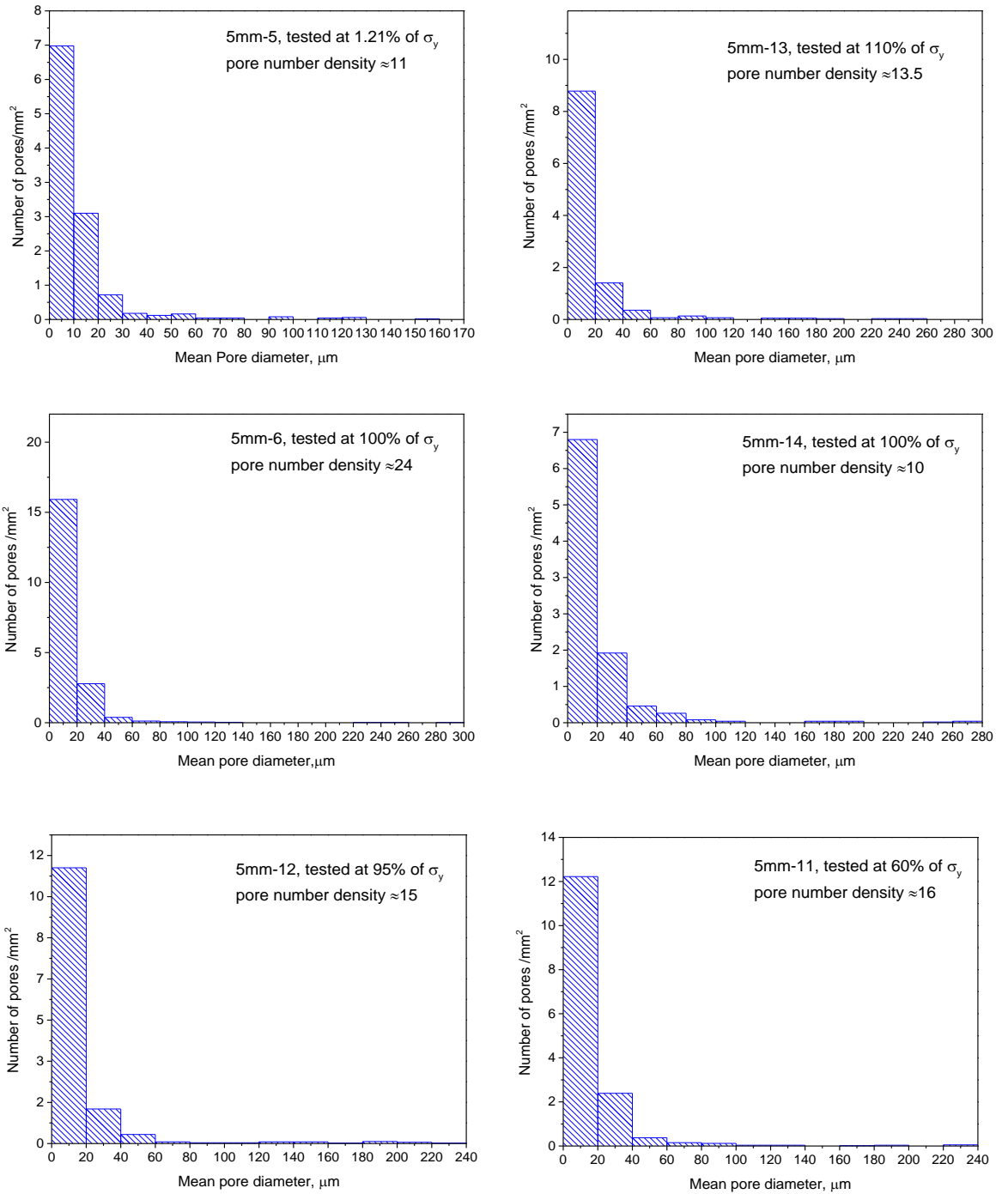
Figure 3.8 Mean pore diameter and number densities of 5 mm samples that were tested at high stress level, sample No.11 tested at 60% of yield stress, which is the fatigue limit.
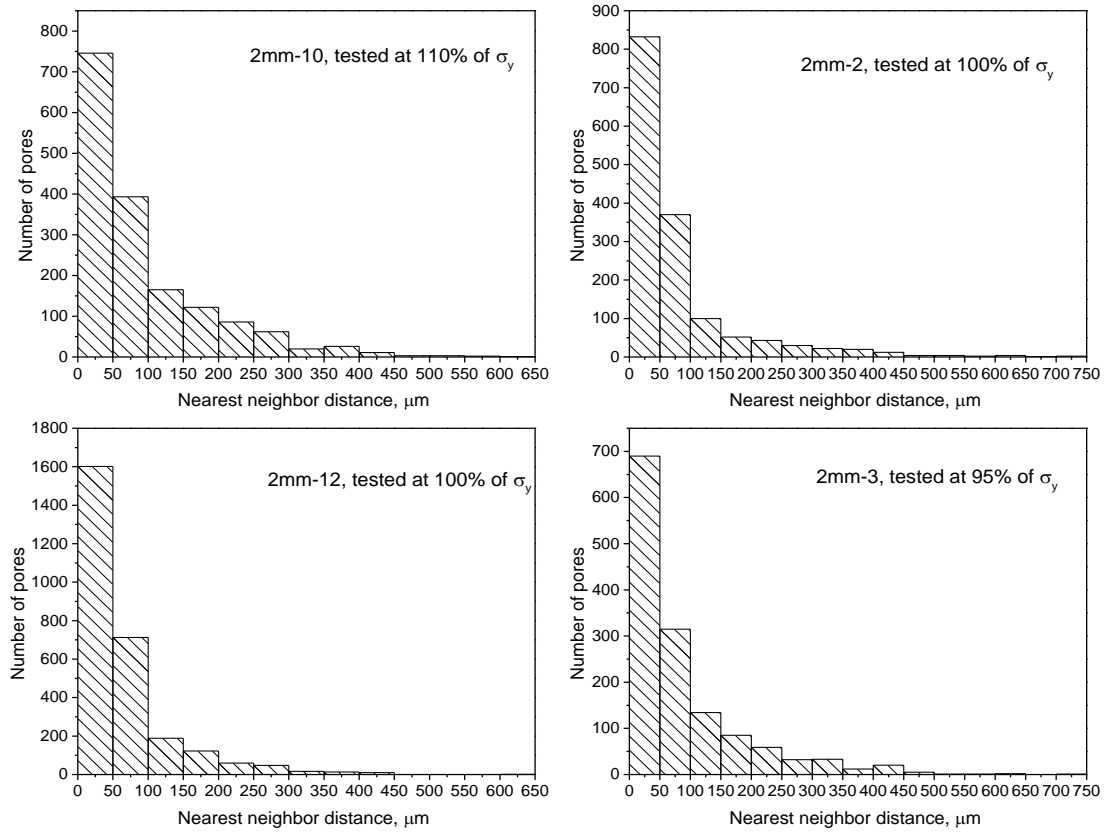
Figure 3.9 Histograms for the nearest nghbor distances between pores in 2mm samples; for samples that were tested at high stress level.
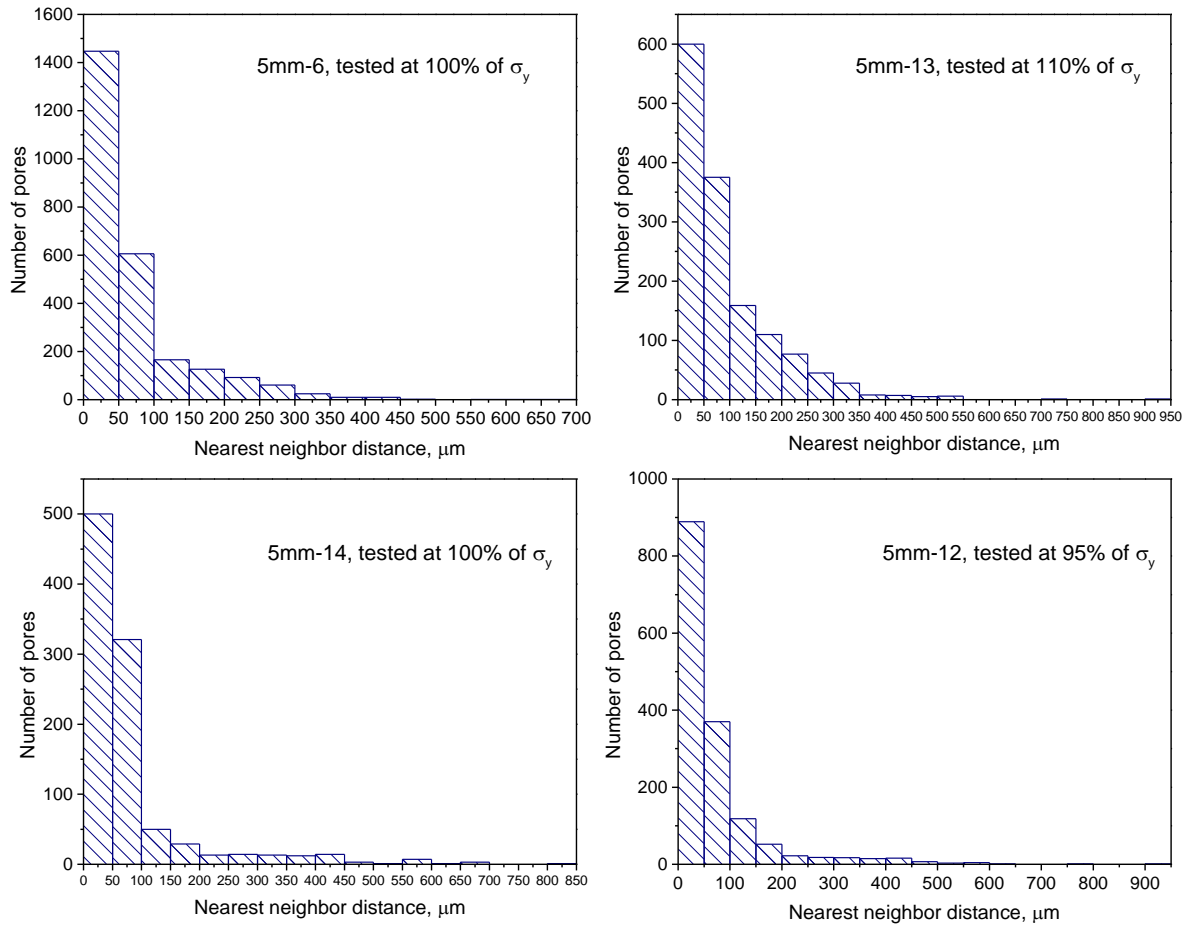
Figure 3.10 Histograms for the nearest nghbor distances between pores in 5 mm
samples; for samples that were tested at high stress levels.

Table 3.1 Summary of statistical results of pore size and distribution in 2 mm samples.
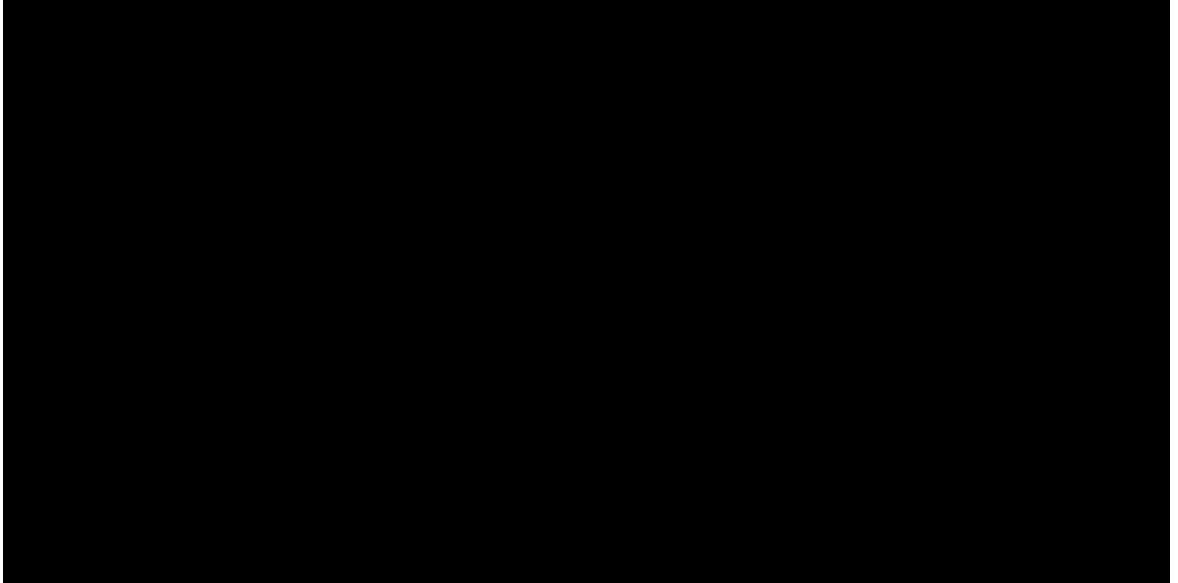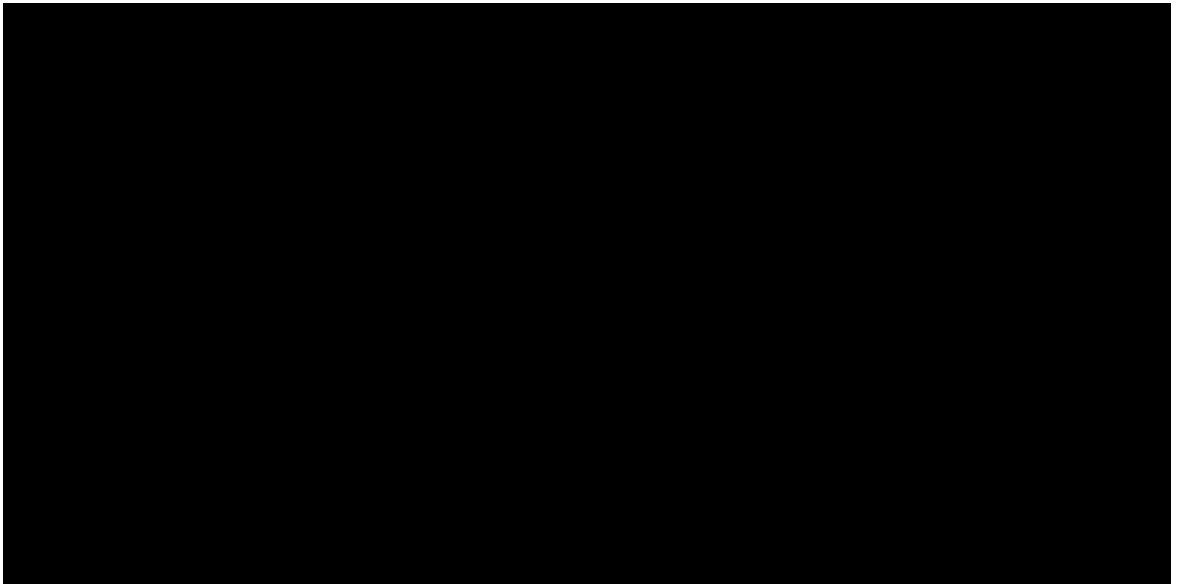
Table 3.2 Summary of statistical results of pore size and distribution in 5 mm samples.
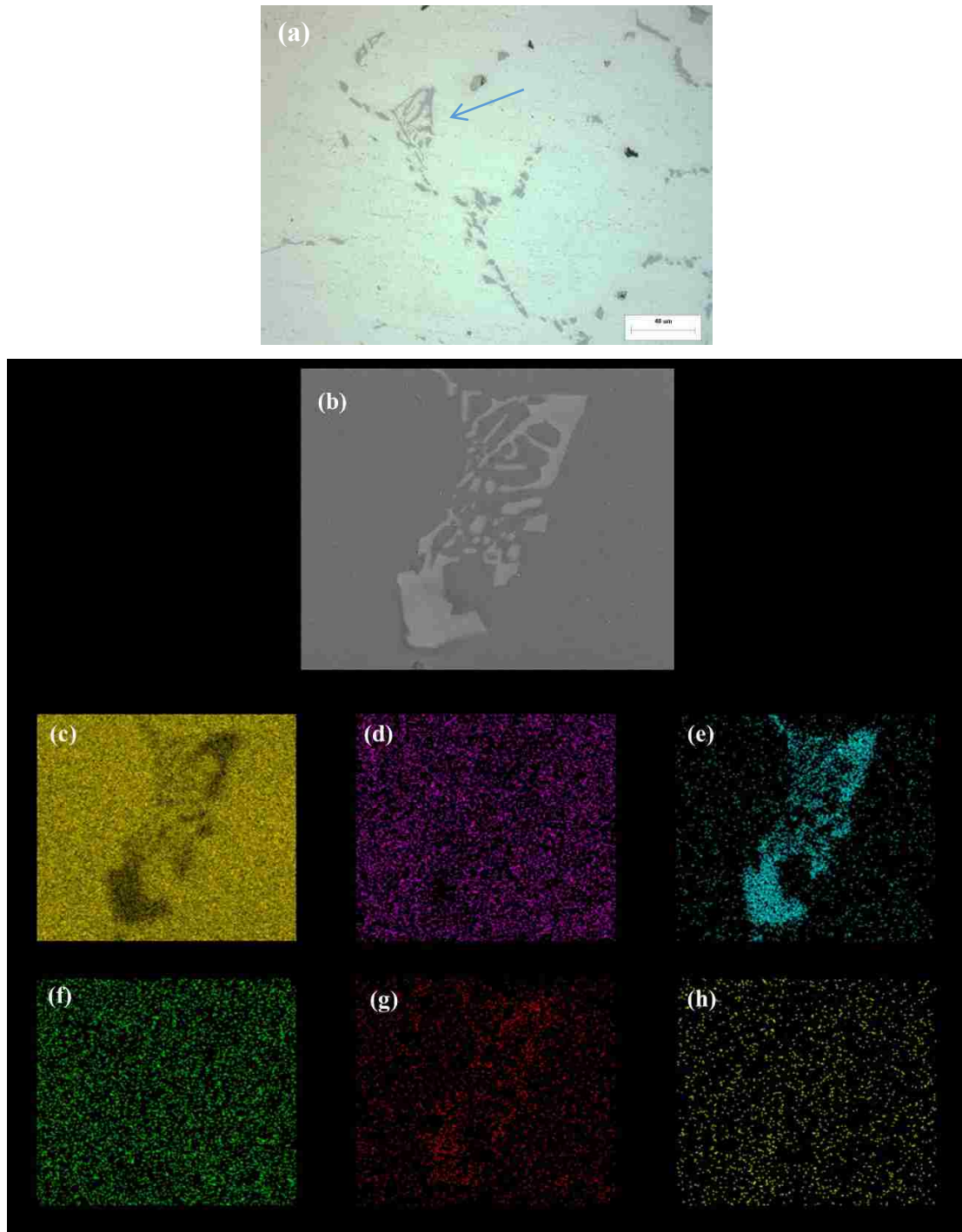
Figure 3.11 Optical micrograph, SEM micrograph, and EDS analysis of the eutectic phase: (a) optical micrograph showing the Fe-particle (a) SEM micrograph of Eutectic particle and EDS maps of (b) aluminum; (c) magnesium; (d) iron; (e) zinc; (f) Manganese; and (g) silicon.
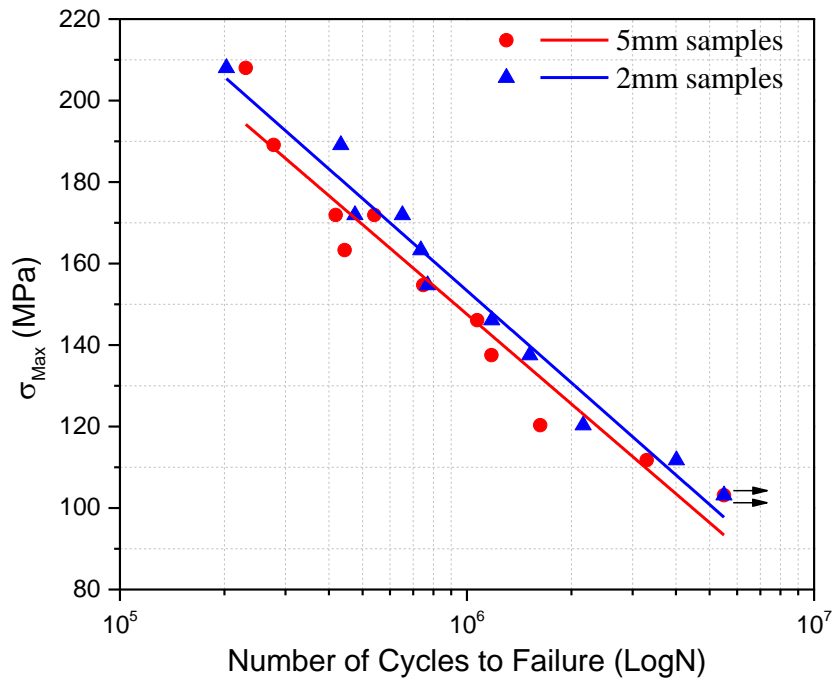
Figure 3.12 S-N curves of the 2mm and 5 mm samples in A713 cast Al alloy by four-point bend fatigue testing.
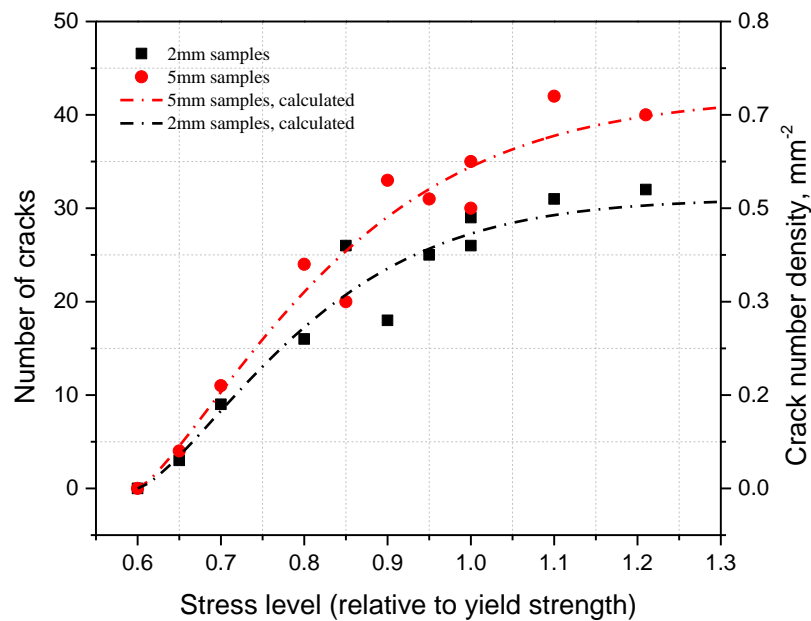
Figure 3.13 Plots of crack population vs. stress level in 2 mm and 5 mm samples of A713 Al alloy.
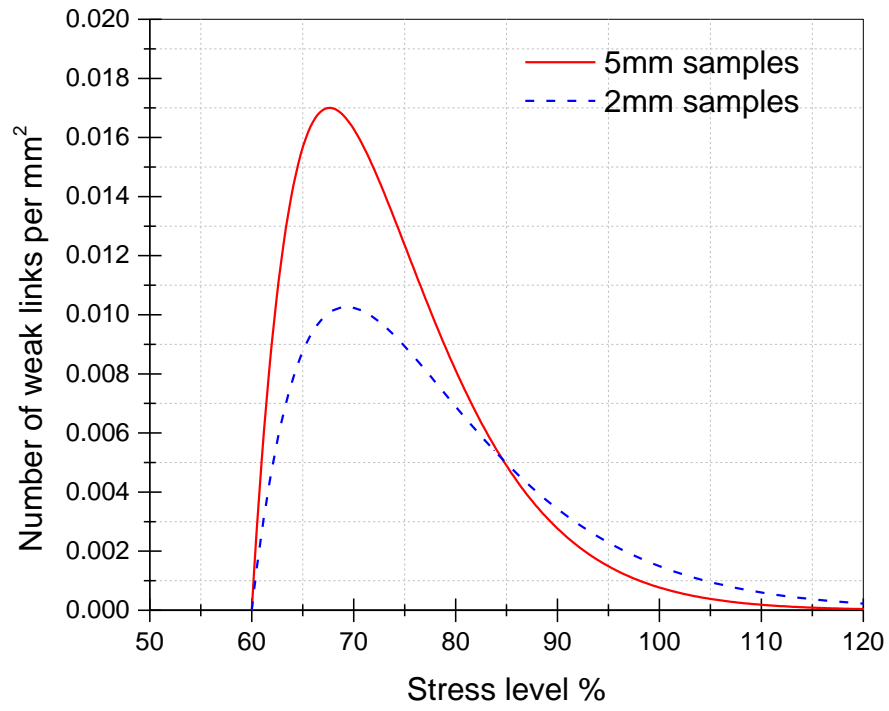
Figure 3.14 Strength distribution of fatigue weak links in 5 mm and 2 mm samples of A713 Al Alloy.
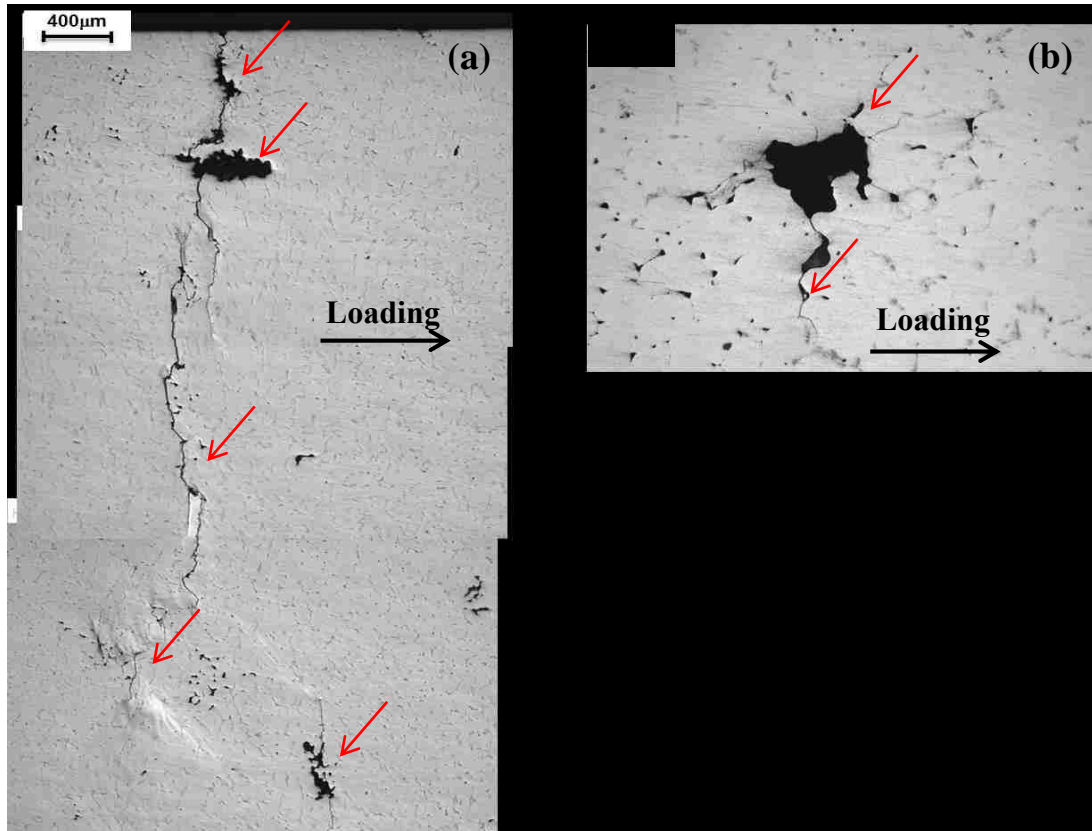
Figure 3.15 (a) multiple fatigue crack nucleation at a high stress level in 5 mm sample, maximum cyclic stress= 110% σ_y; (b) lower fatigue crack initiation sites in 5 mm at a maximum stress level = 65% σ_y, arrows indicate cracks which were nucleated at pores.

Figure 3.16 (a) multiple fatigue crack nucleation at a high stress level in 2 mm sample, maximum cyclic stress= 110% σ_y ; (b) clustered pore; (c) single crack initiation in 2 mm at a maximum stress level = 65% $\sigma_{y.}$, arrows indicate cracks which were nucleated at pores.
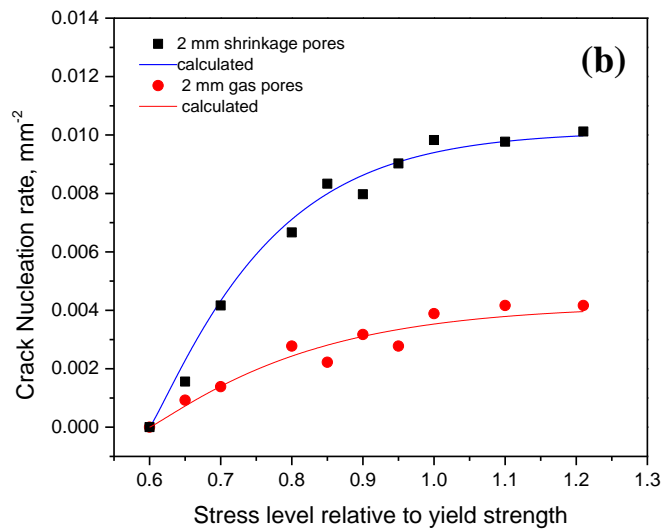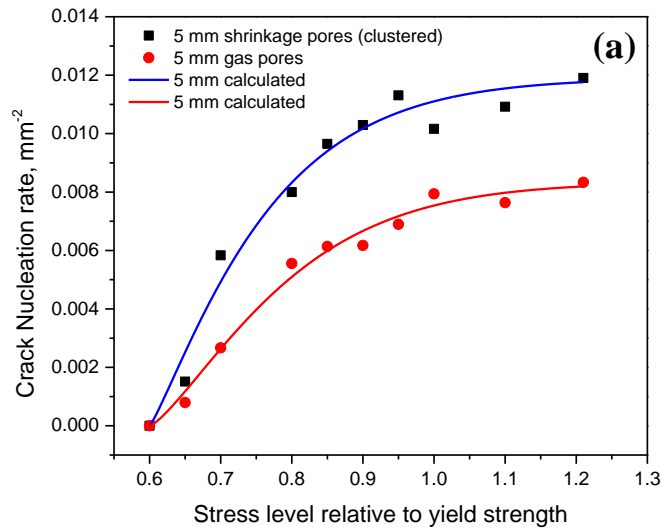
Figure 3.17 Crack nucleation rates of 5 mm and 2 mm samples: (a) crack nucleation rates normalized by pore densities of gas pores and shrinkage pores in 5 mm samples; (b) crack nucleation rates normalized by pore densities of gas pores and shrinkage pores in 2 mm samples.
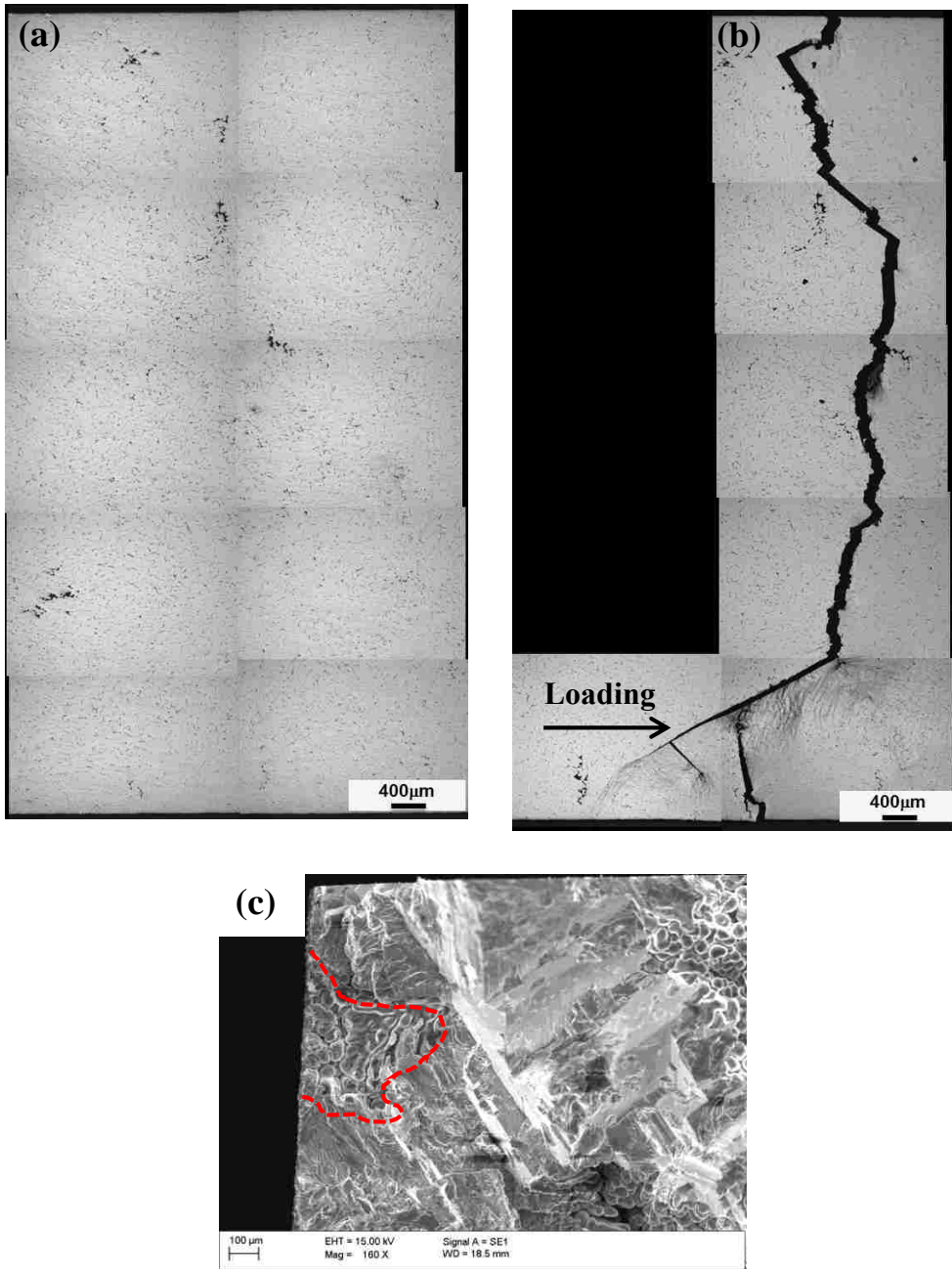
Figure 3.18 Optical micrographs (a) before fatigue test; (b) after fatigue test; and (c) fracture surface showing the main crack initiation site (pore), 110% σ_y, sample No. 2 mm-10.
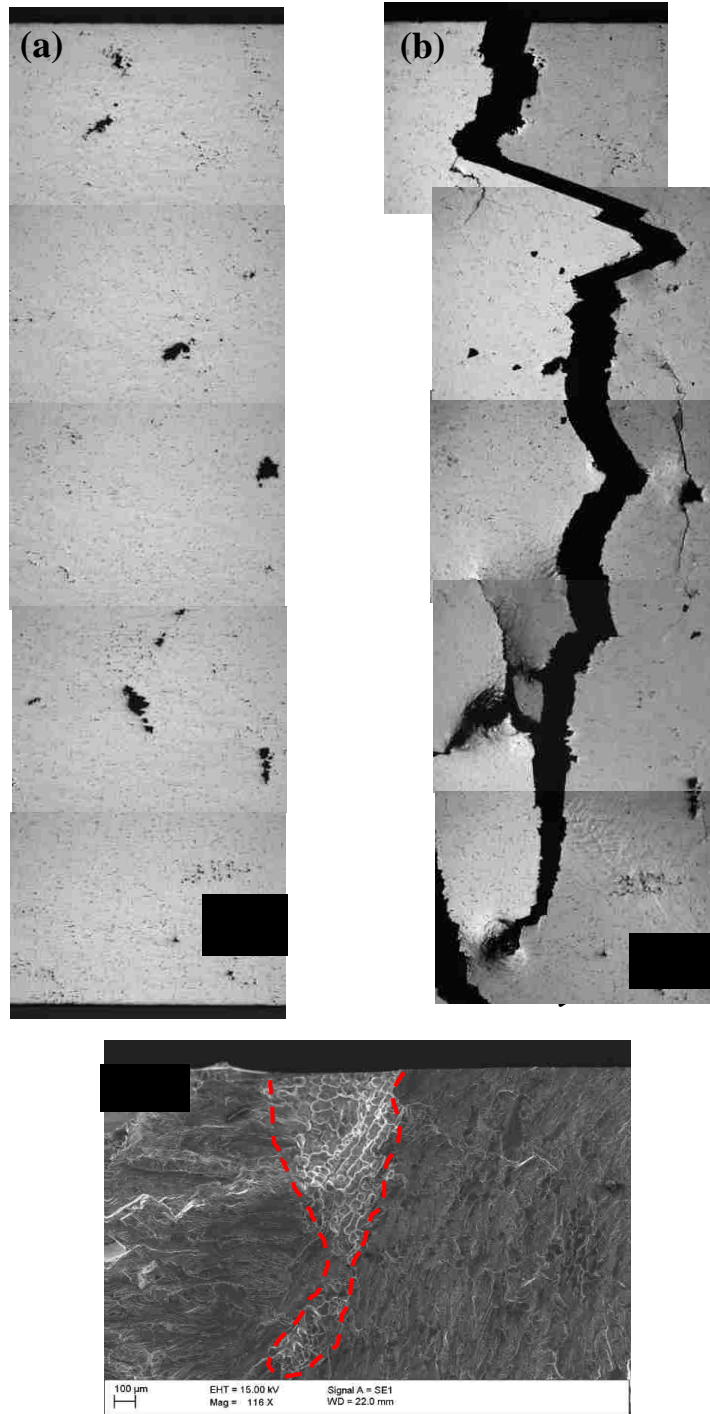
Figure 3.19 Optical micrographs: (a) before fatigue test; (b) after fatigue test; and (c) fracture surface, showing a crack that nucleated at pore, 100% σ_y, sample No. 5 mm-6.
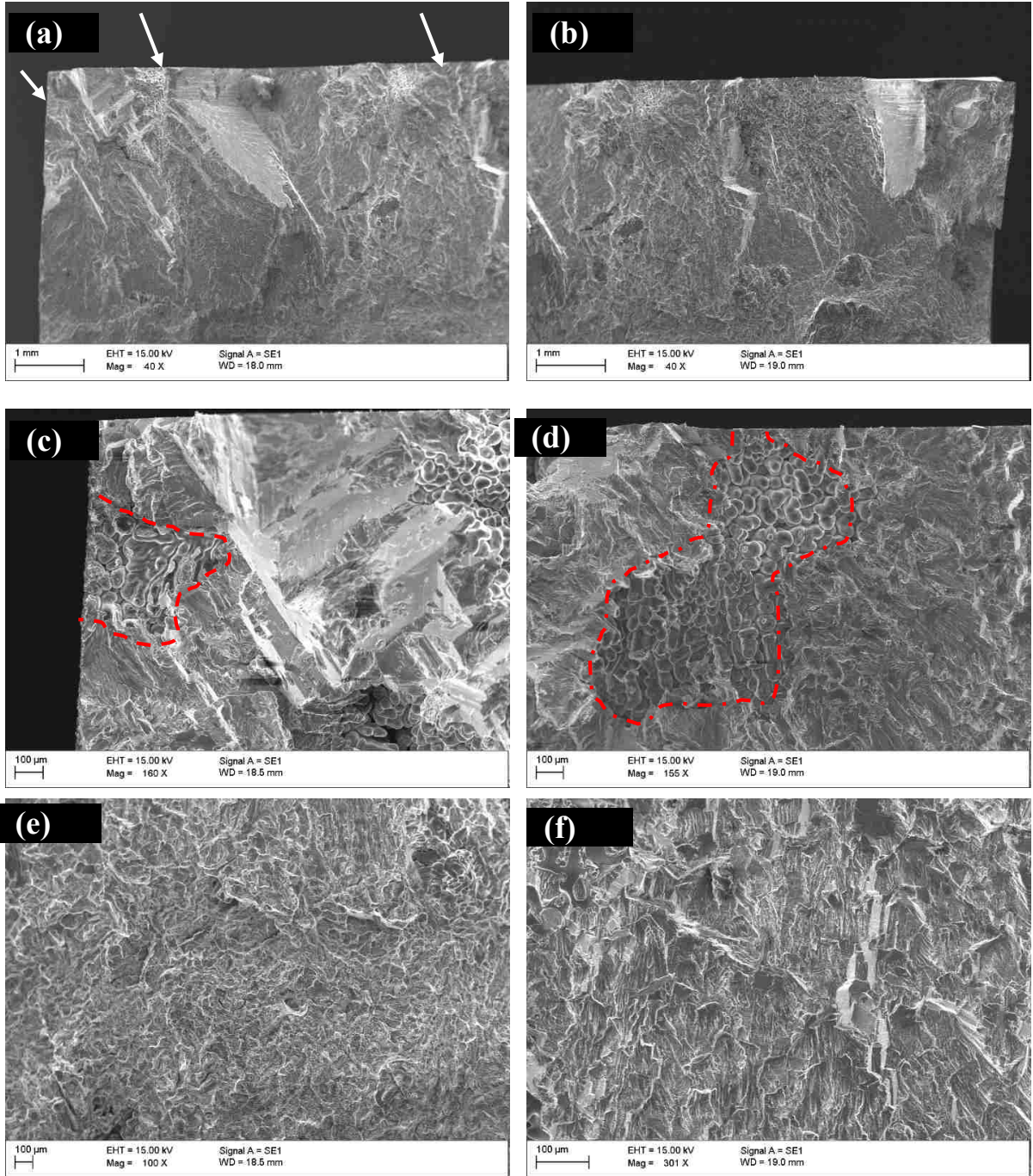
Figure 3.20 SEM micrographs showing: (a) low magnification of fracture surface; (b) the other portion of fracture surface of sample No. 2mm-10, 110% σ_y; (c), and (d) pores nucleated cracks; (e) Crack propagation zone; and (f) final failure.
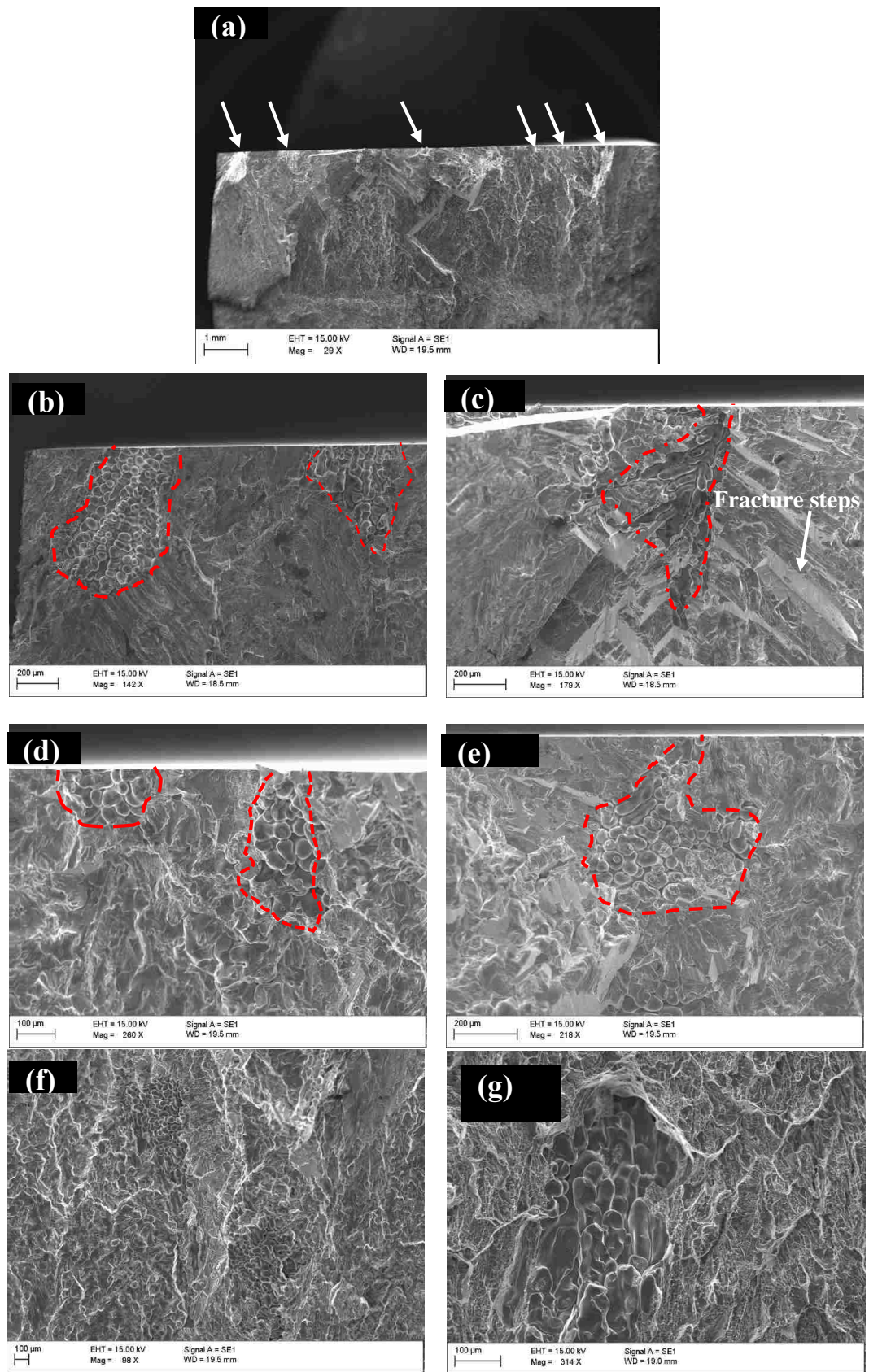
Figure 3.21 SEM micrographs showing (a) low magnification of fracture surface of sample No. 2mm-12, 100% $\sigma_{y;}$ (b),(c),(d), and (e) pores as a crack nucleation sites; (f) crack propagation zone; and (g) final failure.
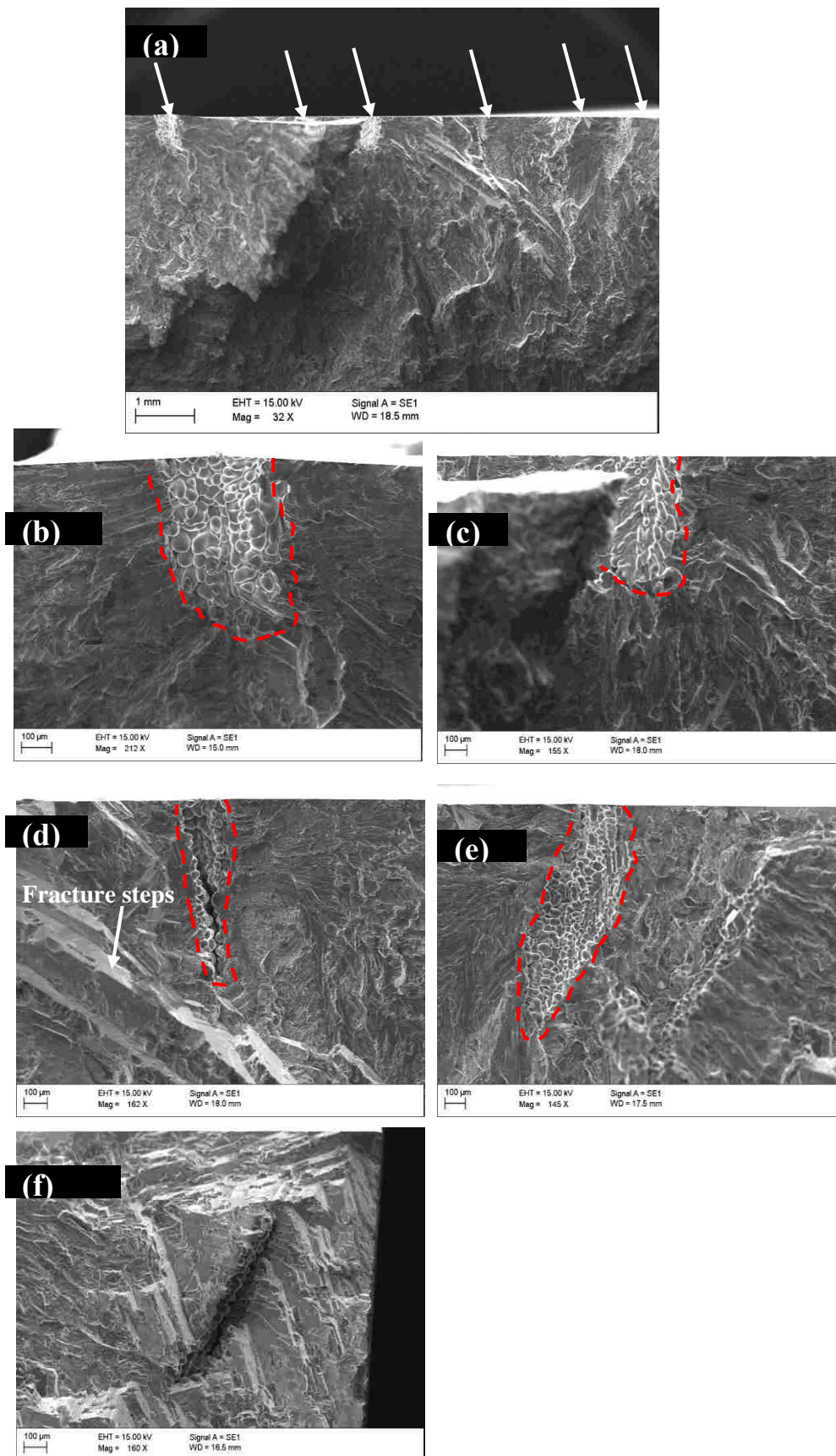
Figure 3.22 SEM micrographs showing (a) low magnification of fracture surface of sample No. 5 mm-13, 110% σ_y; (b),(c),(d), (e) and (f) pores as a crack nucleation sites.
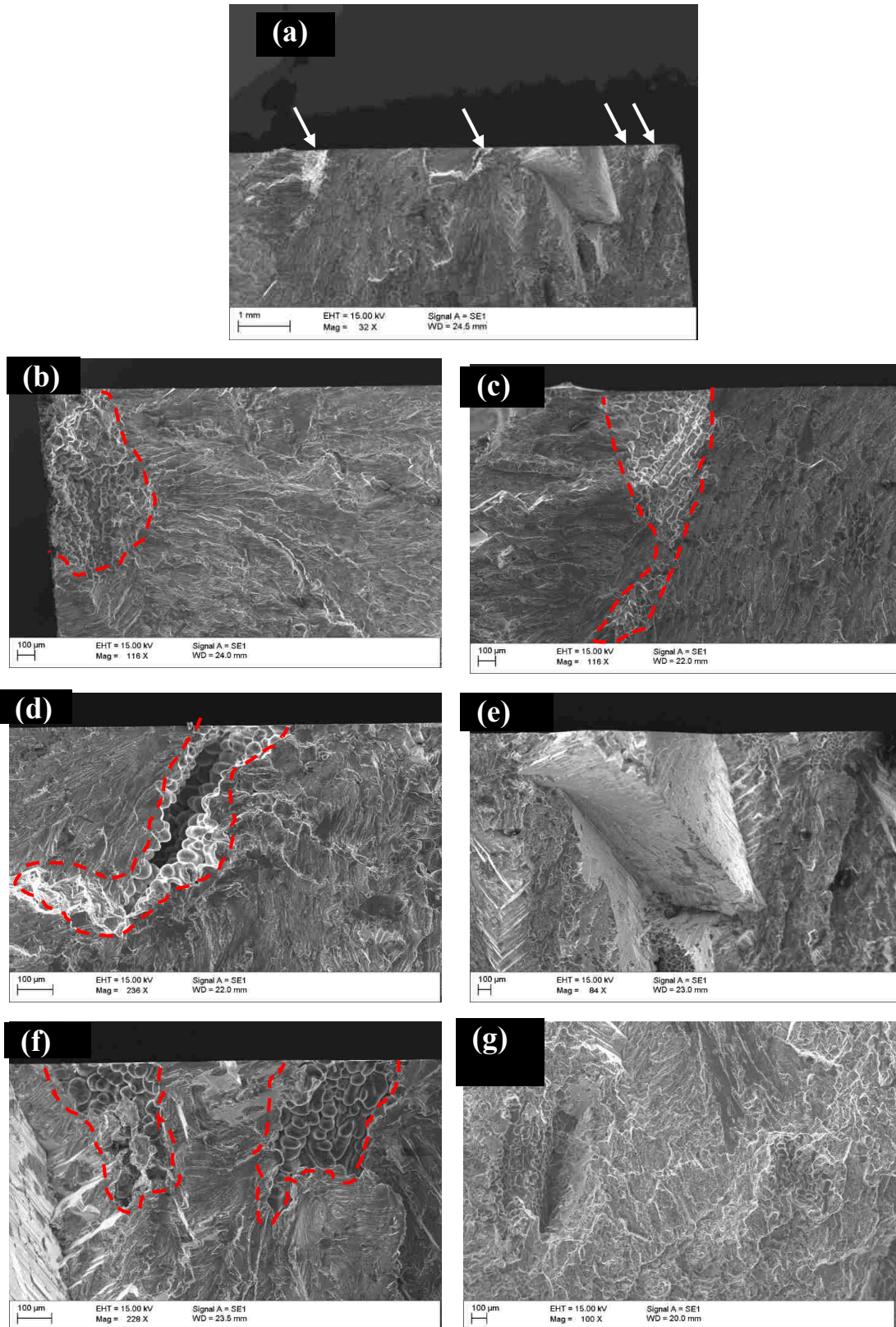
Figure 3.23 SEM micrographs showing (a) low magnification of fracture surface of sample No. 5 mm-6, 100% σ_y; (b),(c),(d), (e), and (f) pores as a crack nucleation sites; and (g) final failure.

Table 3.3 Pore measurements of depth, width, and aspect ratio on the main cracks of the fatigued samples.

Sample 2 mm-10, 110% σ_y				Sample 2 mm-12, 100% σ_y			
Pore No.	Depth, μm	Width μm	Aspect ratio	Pore No.	Depth μm	Width μm	Aspect ratio
1	586	403	0.687	1	688	319	0.463
2	770	344	0.446	2	420	280	0.667
3	456	290	0.636	3	676	362	0.535
4	1012	382	0.377	4	623	411	0.659
				5	478	291	0.608
				6	137	178	1.299
Sample 5 mm-13, 110% σ_y				Sample 5 mm-6, 100% σ_y			
Pore No.	Depth μm	Width μm	Aspect ratio	Pore No.	Depth, μm	Width μm	Aspect ratio
1	586	311	0.530	1	1056	491	0.465
2	544	422	0.775	2	1402	629	0.448
3	681	169	0.248	3	680	198	0.291
4	1024	348	0.334	4	410	296	0.722
5	1110	376	0.338	5	489	271	0.554
				6	1159	562	0.484

Chapter 4 Conclusion

From the investigation into the effect of pore density and distribution on fatigue weak links in an A713 Al alloy, better fatigue lives can be obtained by controlling pore sizes and density during solidification of the melt. Moreover, based on the results presented earlier, the following conclusions can be drawn:

(1) Gas pores and shrinkage pores (clustered), were characterized in an A713 cast aluminum alloy in 2 mm and 5 mm in depth. The mean pore diameter of the 2 mm samples was measured to be between 10 to 14 μm, and the measured mean pore diameters of 5 mm samples were measured to be 14 to 32 μm.

(2) Pore number densities of the 2 mm samples range from 8 to 25 mm^{-2}, while the pore number densities of the 5 mm samples were between 7 to 24 mm^{-2}.

(3) The fatigue lives at high stress levels for the 5 mm samples were lower than those samples of the 2 mm surface.

(4) Crack population vs. stress level plot (i.e. fatigue weak links), shows a Weibull function in an A713 cast aluminum alloy, which is consistent with the previous study. Crack nucleation rates when normalized by pore densities of gas pores and shrinkage pores, the rates show a good fit with Weibull function in the 5 mm samples and in the 2 mm samples as well.

(5) Higher crack nucleation rates of gas pores and shrinkage pores observed in 5 mm samples compared to those in 2 mm samples.

(6) The peak of strength distribution of fatigue weak link density of 5 mm and 2 mm samples were measured to be 0.017 mm^{-2} at 67.6 % σ_y, and 0.01027 mm^{-2} at 69.5% σ_y.

(7) Fractured surfaces reveal that pores are the main crack initiators and the higher the stress level, the greater the number of fatigue weak links. The depth of pores plays a significant role in increasing the stress concentration, which increases the driving force for cracks to nucleate.

(8) Cracks may not necessarily start from coarse pores, but from shrinkage pores (clusters).

(9) Some of the pores on the fractured surfaces in 5 mm samples have aspect ratios of less than 0.7, which indicate that these pores are elongated in the surface and have a narrow width.

4.1 Future Work

Fatigue properties of engineering alloys have been extensively studied. However, cast aluminum alloys need more attention to include all factors that contribute to fatigue crack initiation and early crack growth. The following remarks are suggested for future studies of the fatigue properties of cast Al alloys:

1. It will be interesting to study weather fatigue cracks nucleate at Fe-containing particle, or it might be pores that are buried beneath the particle, shown in figures 4.1 and 4.2, thus, an investigation could to be carried out to find whether these particles significantly contribute to fatigue crack initiation in this cast alloy.

2. It is desirable to understand the effects of 3-dimenssional geometry of shrinkage pores and gas pores on fatigue crack initiation thoroughly in cast Al alloys.

3. Fatigue crack may tend to propagate at preferred slip planes, shown in figure 4.3. It will be appealing to study why these fatigue cracks propagate on particular slip planes.

4. Further work can be accomplished to investigate the effect of solidification time and hydrogen content on pore formation, and from that one can achieve the optimum solidification time, and thus, reduces the amount of pores for better fatigue performance.

5. One can investigate the effect of pores on the surface of the cast blade rather than in depth to quantify pore sizes and distribution and their effect on fatigue properties.
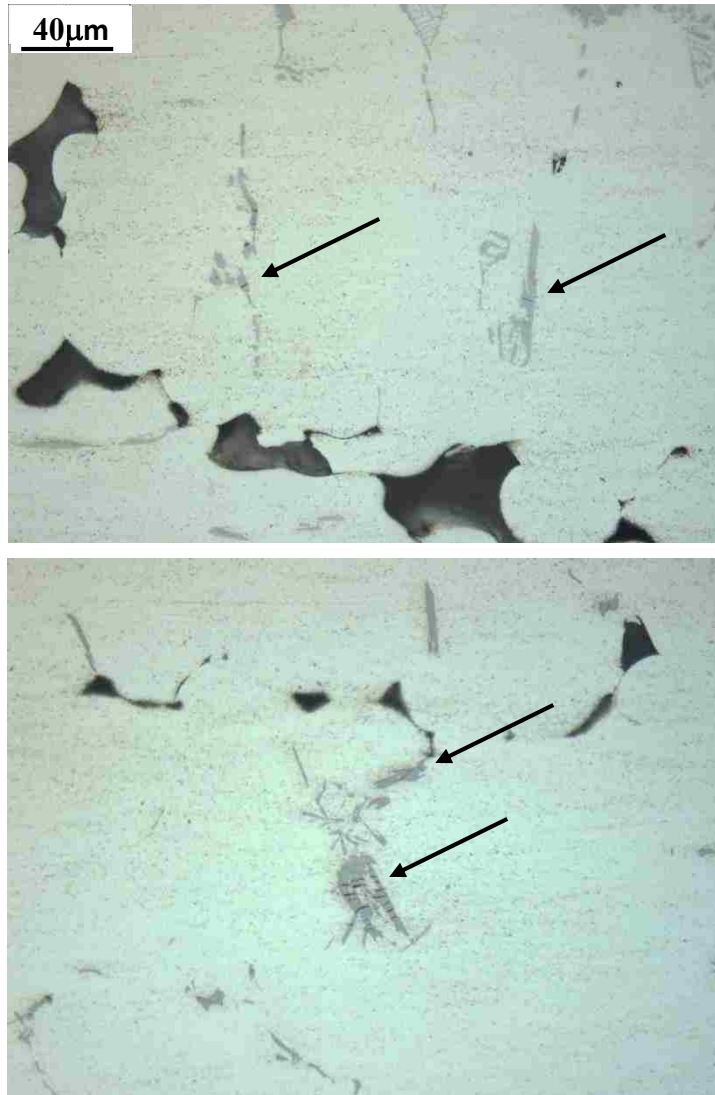
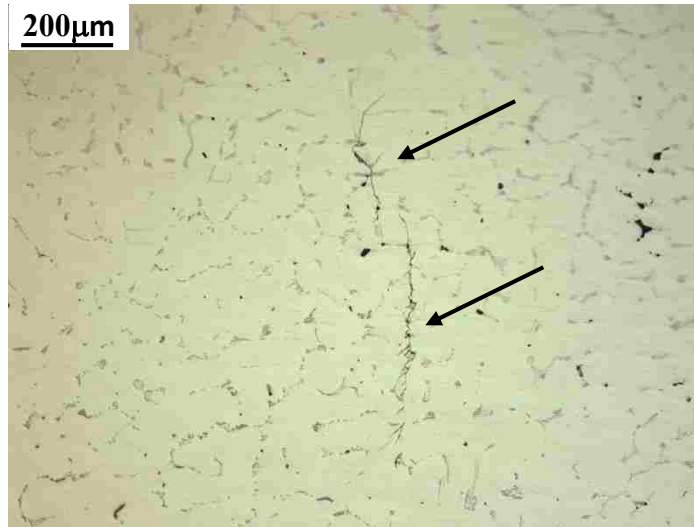Figure 4.1 Optical micrograph showing particles that might pre-fractured before fatigue testing.

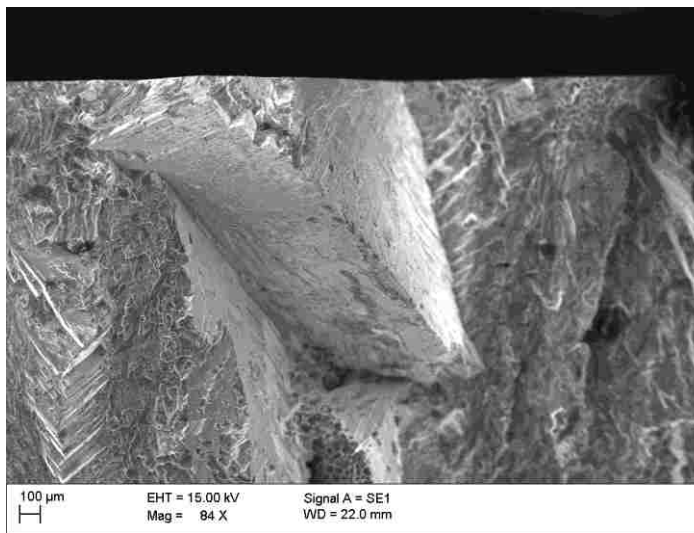Figure 4.2 Cracks that might be nucleated from Fe-containing particles.

Figure 4.3 Crack propagation on a particular slip planes.

References

[1]   J. Schijve, *Fatigue of structures and materials*: Springer, 2001.

[2]   S. Suresh, *Fatigue of materials*: Cambridge university press, 1998.

[3]   W. T. Becker, R. J. Shipley, S. Lampman, B. R. Sanders, S. D. Henry, G. J. Anton*, et al.*, *ASM Handbook: Failure Analysis and Prevention*: ASM International, 2002.

[4]   G. R. Halford, *Fatigue and durability of structural materials*: Asm International, 2006.

[5]   R. I. Stephens, A. Fatemi, R. R. Stephens, and H. O. Fuchs, *Metal fatigue in engineering*: John Wiley & Sons, 2000.

[6]   A. Wöhler, "Versuche über die Festigkeit der Eisenbahnwagenachsen," *Zeitschrift für Bauwesen,* vol. 10, pp. 160-161, 1860.

[7]   J. Ewing and J. Humfrey, "The fracture of metals under repeated alternations of stress," *Philosophical Transactions of the Royal Society of London. Series A, Containing Papers of a Mathematical or Physical Character,* vol. 200, pp. 241-250, 1903.

[8]   O. Basquin, "The exponential law of endurance tests," in *proc. ASTM*, 1910, p. 625.

[9]   P. C. Paris and F. Erdogan, "A critical analysis of crack propagation laws," 1963.

[10]   P. C. Paris, M. P. Gomez, and W. E. Anderson, "A rational analytic theory of fatigue," *The trend in engineering,* vol. 13, pp. 9-14, 1961.

[11]   N. Thompson, N. Wadsworth, and N. Louat, "Xi. The origin of fatigue fracture in copper," *Philosophical Magazine,* vol. 1, pp. 113-126, 1956.

[12]   C. Zapffe and C. Worden, "Fractographic registrations of fatigue," *Transactions of the American Society for Metals,* vol. 43, pp. 958-969, 1951.

[13]   P. Forsyth and D. Ryder, "Fatigue Fracture: Some Results Derived from the Microscopic Examination of Crack Surfaces," *Aircraft Engineering and Aerospace Technology,* vol. 32, pp. 96-99, 1960.

[14]   P. Forsyth, "Fatigue Crack Formation in Silver Chloride," in *Symposium on Basic Mechanisms of Fatigue*, 1959.

[15]   P. Forsyth, "Slip-band damage and extrusion," in *Proceedings of the Royal Society of London A: Mathematical, Physical and Engineering Sciences*, 1957, pp. 198-202.

[16]   H. Cummings, F. Stulen, and W. Schulte, "Tentative fatigue strength reduction factors for silicate-type inclusions in high-strength steels," in *Proc. ASTM*, 1958, p. 505.

[17]   A. Standard, "E466: Standard Practice for Conduction Force Controlled Constant Amplitude Axial Fatigue Test of Metallic Materials, vol. 03.01," *Annual Book of ASTM Standards, West Conshohocken,* 2002.

[18]   K. Katagiri, A. Omura, K. Koyanagi, J. Awatani, T. Shiraishi, and H. Kaneshiro, "Early stage crack tip dislocation morphology in fatigued copper," *Metallurgical Transactions A,* vol. 8, pp. 1769-1773, 1977.

[19]   U. Krupp, *Fatigue crack propagation in metals and alloys: microstructural aspects and modelling concepts*: John Wiley & Sons, 2007.

[20]   D. McDowell and F. Dunne, "Microstructure-sensitive computational modeling of fatigue crack formation," *International journal of fatigue,* vol. 32, pp. 1521-1542, 2010.

[21]   K. S. Chan, P. Jones, and Q. Wang, "Fatigue crack growth and fracture paths in sand cast B319 and A356 aluminum alloys," *Materials Science and Engineering: A,* vol. 341, pp. 18-34, 2003.

[22]   R. McCammon and H. Rosenberg, "The Fatigue and Ultimate Tensile Strengths of Metals between 4.2 and 293 degrees K," in *Proceedings of the Royal Society of London A: Mathematical, Physical and Engineering Sciences*, 1957, pp. 203-211.

[23]   D. A. Lados and D. Apelian, "Fatigue crack growth characteristics in cast Al–Si–Mg alloys: Part I. Effect of processing conditions and microstructure," *Materials Science and Engineering: A,* vol. 385, pp. 200-211, 2004.

[24]   S. Axter, W. B. Jones, and D. Polonis, "Microstructural origins of dynamic fracture in 2024 aluminum alloy," *Metallography,* vol. 8, pp. 425-438, 1975.

[25]   E. DeBartolo and B. Hillberry, "Effects of constituent particle clusters on fatigue behavior of 2024-T3 aluminum alloy," *International Journal of Fatigue,* vol. 20, pp. 727-735, 1998.

[26]   C. B. Fuller, A. R. Krause, D. C. Dunand, and D. N. Seidman, "Microstructure and mechanical properties of a 5754 aluminum alloy modified by Sc and Zr additions," *Materials Science and Engineering: A,* vol. 338, pp. 8-16, 2002.

[27]   Y. Jin, P. Cai, W. Wen, H. Nagaumi, B. Xu, Y. Zhang*, et al.*, "The anisotropy of fatigue crack nucleation in an AA7075 T651 Al alloy plate," *Materials Science and Engineering: A,* vol. 622, pp. 7-15, 2015.

[28]   J. G. Kaufman and E. L. Rooy, *Aluminum alloy castings: properties, processes, and applications*: Asm International, 2004.

[29]   M. Handbook, "Casting, vol. 15," *ASM International,* pp. 238-241, 1988.

[30]   H. Ammar, A. Samuel, and F. Samuel, "Effect of casting imperfections on the fatigue life of 319-F and A356-T6 Al–Si casting alloys," *Materials Science and Engineering: A,* vol. 473, pp. 65-75, 2008.

[31]   J. M. Boileau and J. E. Allison, "The effect of porosity size on the fatigue properties in a cast 319 aluminum alloy," SAE Technical Paper 0148-7191, 2001.

[32]   M. Avalle, G. Belingardi, M. P. Cavatorta, and R. Doglione, "Casting defects and fatigue strength of a die cast aluminium alloy: a comparison between standard specimens and production components," *International journal of Fatigue,* vol. 24, pp. 1-9, 2002.

[33]   A. Samuel and F. Samuel, "Porosity and the fatigue behavior of hypoeutectic and hypereutectic aluminum–silicon casting alloys," *International journal of Fatigue,* vol. 30, pp. 1024-1035, 2008.

[34]   A. Handbook, *Casting* vol. 15. Materials Park: ASM International, 2008.

[35]   J. Campbell, *Complete casting handbook: metal casting processes, metallurgy, techniques and design*: Butterworth-Heinemann, 2015.

[36]   J. Anson and J. Gruzleski, "The quantitative discrimination between shrinkage and gas microporosity in cast aluminum alloys using spatial data analysis," *Materials Characterization,* vol. 43, pp. 319-335, 1999.

[37]   A. Tewari, M. Dighe, and A. M. Gokhale, "Quantitative characterization of spatial arrangement of micropores in cast microstructures," *Materials characterization,* vol. 40, pp. 119-132, 1998.

[38]   Y. Zhang, J. Xu, and T. Zhai, "Distributions of pore size and fatigue weak link strength in an A713 sand cast aluminum alloy," *Materials Science and Engineering: A,* vol. 527, pp. 3639-3644, 2010.

[39]   J. Zhang, M. A. Przystupa, and A. J. Luévano, "Characterizations of pore and constituent particle populations in 7050-T7451 aluminum plate alloys," *Metallurgical and Materials Transactions A,* vol. 29, pp. 727-737, 1998.

[40]   P. Mu, Y. Nadot, C. Nadot-Martin, A. Chabod, I. Serrano-Munoz, and C. Verdu, "Influence of casting defects on the fatigue behavior of cast aluminum AS7G06-T6," *International Journal of Fatigue,* vol. 63, pp. 97-109, 2014.

[41]   D. Lados, D. Apelian, and A. De Figueredo, "Fatigue performance of high integrity cast aluminum components," in *Proceedings from the 2nd international aluminum casting technology symposium*, 2002, pp. 185-96.

[42]   C. Sonsino and J. Ziese, "Fatigue strength and applications of cast aluminium alloys with different degrees of porosity," *International Journal of Fatigue,* vol. 15, pp. 75-84, 1993.

[43]   J.-Y. Buffière, S. Savelli, P.-H. Jouneau, E. Maire, and R. Fougeres, "Experimental study of porosity and its relation to fatigue mechanisms of model Al–Si7–Mg0. 3 cast Al alloys," *Materials Science and Engineering: A,* vol. 316, pp. 115-126, 2001.

[44]   J. Fan, D. L. McDowell, M. F. Horstemeyer, and K. Gall, "Cyclic plasticity at pores and inclusions in cast Al–Si alloys," *Engineering Fracture Mechanics,* vol. 70, pp. 1281-1302, 2003.

[45]   T. Zhai, "Strength distribution of fatigue crack initiation sites in an Al-Li alloy," *Metallurgical and Materials Transactions A,* vol. 37, pp. 3139-3147, 2006.

[46]   A. Balasundaram and A. Gokhale, "Quantitative characterization of spatial arrangement of shrinkage and gas (air) pores in cast magnesium alloys," *Materials Characterization,* vol. 46, pp. 419-426, 2001.

[47]   G. Nikiforov, "Metallurgy of fusion welding aluminium alloys," *Moscow: Mashinostroenie,* p. 264, 1972.

[48]   K. Kubo and R. D. Pehlke, "Mathematical modeling of porosity formation in solidification," *Metallurgical Transactions B,* vol. 16, pp. 359-366, 1985.

[49]   J. Campbell, "Feeding mechanisms in castings," *AFS Cast Metals Research Journal,* vol. 5, pp. 1-8, 1969.

[50]   R. Atwood, S. Sridhar, and P. Lee, "Equations for nucleation of hydrogen gas pores during solidification of aluminium seven weight percent silicon alloy," *Scripta materialia,* vol. 41, pp. 1255-1259, 1999.

[51]   A. Knuutinen, K. Nogita, S. McDonald, and A. Dahle, "Porosity formation in aluminium alloy A356 modified with Ba, Ca, Y and Yb," *Journal of Light Metals,* vol. 1, pp. 241-249, 2001.

[52]   K. Tynelius and J. Major, "A parametric study of microporosity in the A356 casting alloy system," *TRANSACTIONS-AMERICAN FOUNDRYMENS SOCIETY,* pp. 401-401, 1993.

[53]   D. Stefanescu and A. Catalina, "Physics of microporosity formation in casting alloys–sensitivity analysis for Al–Si alloys," *International Journal of Cast Metals Research,* vol. 24, pp. 144-150, 2011.

[54]   J. Friedli, J. L. Fife, P. Di Napoli, and M. Rappaz, "X-ray tomographic microscopy analysis of the dendrite orientation transition in Al-Zn," in *IOP Conference Series: Materials Science and Engineering*, 2012, p. 012034.

[55]   P. N. Anyalebechi, "Hydrogen-induced gas porosity formation in Al–4.5 wt% Cu–1.4 wt% Mg alloy," *Journal of Materials Science,* vol. 48, pp. 5342-5353, 2013.

[56]   H. Yin and J. N. Koster, "In-situ observed pore formation during solidification of aluminium," *ISIJ international,* vol. 40, pp. 364-372, 2000.

[57]   R. Atwood, S. Sridhar, W. Zhang, and P. Lee, "Diffusion-controlled growth of hydrogen pores in aluminium–silicon castings: in situ observation and modelling," *Acta materialia,* vol. 48, pp. 405-417, 2000.

[58]   Q. Fang and D. Granger, "Porosity formation in modified and unmodified A356 alloy castings," *AFS Trans,* vol. 97, pp. 989-1000, 1989.

[59]   Z. Xu, W. Wen, and T. Zhai, "Effects of pore position in depth on stress/strain concentration and fatigue crack initiation," *Metallurgical and Materials Transactions A,* vol. 43, pp. 2763-2770, 2012.

[60]   T. Zhai, Y. Xu, J. Martin, A. Wilkinson, and G. Briggs, "A self-aligning four-point bend testing rig and sample geometry effect in four-point bend fatigue," *International Journal of Fatigue,* vol. 21, pp. 889-894, 1999.

[61]   D. Brandon and W. D. Kaplan, *Microstructural characterization of materials*: John Wiley & Sons, 2013.

[62]   R. F. Egerton, *Physical principles of electron microscopy*: Springer, 2005.

[63]   W. Zhou and Z. L. Wang, *Scanning microscopy for nanotechnology: techniques and applications*: Springer science & business media, 2007.

VITA

Place of Birth: Makkah, Saudi Arabia

Education:

- University of Kentucky, Lexington, Kentucky

  2015-Present, M.S. (Materials Science and Engineering)

- King Abdulaziz University, Jeddah, Saudi Arabia

  2006-2010, B.S., Mechanical Engineering (Production and Mechanical Systems

  Design)

Employment:

Researcher, King Abdulaziz City for Science and Technology, Riyadh, Saudi Arabia,

08/2011- Present.

Research:

- Fatigue behavior in Al alloys

- Structure-Properties relationship in steels